

The Effect of Measurement Uncertainties on the Inferred Stability of Planes of Satellite Galaxies

Prem Kumar^{1,2}, Marcel S. Pawłowski², Kosuke Jamie Kanehisa^{2,3}, Pengfei Li⁴, Mariana P. Júlio^{2,3} and Salvatore Taibi^{2,5}

¹ Institut für Astrophysik (IfA), Universität Wien, Türkenschanzstraße 17, 1180 Wien
e-mail: prem.kumar@univie.ac.at

² Leibniz-Institut für Astrophysik Potsdam (AIP), An der Sternwarte 16, 14482 Potsdam, Germany
e-mail: mpawłowski@aip.de

³ Institut für Physik und Astronomie Universität Potsdam, Karl-Liebknecht-Straße 24/25, 14476 Potsdam, Germany

⁴ School of Astronomy and Space Science, Nanjing University, Nanjing, Jiangsu 210023, China

⁵ Institute of Physics, Laboratory of Astrophysics, Ecole Polytechnique Fédérale de Lausanne (EPFL), Observatoire de Sauverny, CH-1290 Versoix, Switzerland

Received September 15, 1996; accepted March 16, 1997

ABSTRACT

Context. Observations have revealed that the Milky Way, Andromeda, Centaurus A (and potentially other galaxies) host spatially thin and kinematically coherent planes of satellites. Such structures are highly improbable within the standard Λ CDM cosmological model, and the dynamical stability of these planes has been a subject of debate for a long time. Accurately determining their stability requires a thorough understanding of orbital parameters such as proper motion, distance, and line-of-sight velocity, in addition to the gravitational potential of the host galaxy. However, many of these remain insufficiently constrained, leading to significant uncertainties in any analysis.

Aims. This research aims to explore the impact of measurement errors in proper motions and distances of the satellite galaxies and in the adopted host halo mass on the inferred stability of satellite planes in Milky-Way-like potentials.

Methods. Test satellite galaxies orbiting a host galaxy are simulated, mock observed by adding various degrees and types of observational errors, and then backward-integrated. Trends and correlations between the initial conditions and the applied uncertainties on the inferred orbital stability of the satellite systems are analyzed. Additionally, the effects of adopting incorrect potentials and the impact of different orbital eccentricities are considered.

Results. Uncertainties in proper motions lead to an inferred, ostensible widening of an intrinsically stable satellite plane, with its width increasing linearly with the adopted proper motion uncertainties. Even uncertainties on the level of Gaia systematics strongly affect the plane's inferred past width. Moreover, the potential with a low halo mass showed a significant impact on the stability of these planes, while the remaining two host models showed similar effects. Uncertainties in satellite distance also contribute noticeably to the inferred, apparent instability.

Key words. Galaxies: dwarf; galaxies: evolution; galaxies: kinematics and dynamics; methods: numerical.

1. Introduction

A century ago, astronomers were acquainted with only two prominent satellite galaxies orbiting the Milky Way, the Large Magellanic Cloud (LMC) and the Small Magellanic Cloud (SMC) – a knowledge that had persisted for centuries (von Homboldt & Otte 1997). This celestial census doubled when Shapley (1938) utilized photographic plates and discovered two more dwarfs – Sculptor and Fornax. With the discovery of Sagittarius in 1994, the number of satellite galaxies of the Milky Way reached 11 (Ibata et al. 1994), and has substantially increased due to advancements in observational technology, the deployment of larger telescopes, and systematic sky surveys. Currently, approximately 60 dwarf galaxies have been discovered around the Milky Way (Simon 2019). Notably, it has also been discovered that these bright satellite galaxies of the Milky Way tend to lie on a great circle called the “Magellanic Plane” (Lynden-Bell 1976). Observations have shown that satellite galaxies around the Milky Way are highly anisotropic and kinematically correlated, with most of them being located in a thin plane roughly

perpendicular to the disc of the Milky Way (Kroupa et al. 2005; Metz et al. 2008). The most luminous among these galaxies appear to align within a thin disk-like structure known as the Vast Polar Structure (VPOS, Pawłowski et al. 2012; Taibi et al. 2024). The VPOS exhibits a root mean square (rms) thickness of 20–30 kpc, a radius of about 250 kpc and an axis ratio c/a of 0.18 – 0.30 (Pawłowski 2018, 2021b).

A comparable thin and anisotropic distribution of satellite galaxies around Andromeda, referred to as The Great Plane of Andromeda (GPoA) (Ibata et al. 2013; Conn et al. 2013), and Centaurus A, known as Centaurus A Satellite Plane (CASP) (Tully et al. 2015; Müller et al. 2018; Kanehisa et al. 2023b), was also found. These structures are characterized by an axis ratio of $c/a = 0.1$ (Pawłowski et al. 2013) and c/a ratio = 0.2 (Tully et al. 2015), respectively. Both planes, GPoA and CASP, are reported to have a significant correlation in the line-of-sight velocities of satellite members when observed along the edge-on orientation (Ibata et al. 2013; Müller et al. 2021). This suggests that satellites exhibit a consistent sense of co-rotation, with satellites on one

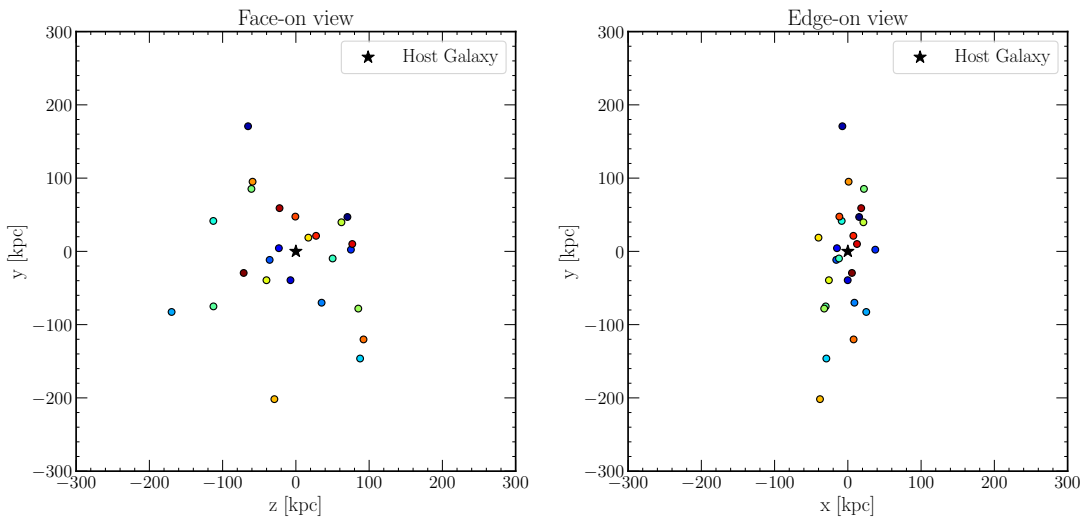


Fig. 1. Face-on (left) and Edge-on (right) views of $N_{\text{sat}} = 25$ randomly generated test satellite points represented by different colors. The star symbol represents the host galaxy.

side of the host predominantly receding and those on the other side approaching relative to the host. The rotating pattern around its host galaxy, akin to the VPOS, thus supports the idea that both the GPOA and CASP constitute a nonrandom and coherent structure. Moreover, the first proper motion measurements for three on-plane satellite galaxies of M31 indicate that these are indeed consistent with co-orbiting along the spatially identified GPOA (Sohn et al. 2020; Pawłowski & Tony Sohn 2021; Casetti-Dinescu et al. 2024). A similar flattened structure with coherent line-of-sight velocities has recently been discovered around the galaxy NGC 4490 and found to be rare in cosmological simulations (Karachentsev & Kroupa 2024; Pawłowski et al. 2024).

1.1. Plane Setup

Today, the Lambda Cold Dark Matter (Λ CDM) cosmological model is widely accepted among researchers due to its ability to explain a range of astrophysical phenomena such as Big Bang Nucleosynthesis, the accelerated expansion of the universe (Riess et al. 1998), the power spectrum of the Cosmic Microwave Background (Spergel et al. 2003), large-scale structure (Peacock et al. 2001; Tegmark et al. 2004) and the matter-energy budget of our universe (Ade et al. 2016). However, on smaller scales it presents several challenges. Among them, the Plane of Satellite Galaxies has persistently been a topic of debate (Pawłowski 2018) and it has been found that such structures are considered highly improbable within the standard Λ CDM cosmological model (Kroupa et al. 2005; Pawłowski 2021b). Several solutions have been suggested to explain this discrepancy; however, none have achieved general consensus. These proposed solutions include the accretion along filaments of the cosmic web (Libeskind et al. 2011; Lovell et al. 2011), in-fall of satellite galaxies in groups (Li & Helmi 2008; D’Onghia & Lake 2008; Metz et al. 2009; Shao et al. 2018; Wang et al. 2013; Júlio et al. 2024), galaxy mergers (Smith et al. 2016; Kanehisa et al. 2023a), effects induced by the infall of a massive LMC (Garavito-Camargo et al. 2021; Pawłowski et al. 2022; Vasiliev 2023), tidal dwarf galaxies (Pawłowski et al. 2011; Fouquet et al. 2012; Banik et al. 2022), and hydrodynamics and baryonic physics (Pawłowski et al. 2015; Ahmed et al. 2017; Müller et al.

2018; Pawłowski et al. 2019). Thus, while each hypothesis contributes valuable insights, a unified explanation remains elusive, highlighting the complexity of galaxy formation and evolution processes.

Investigation of the orbits of satellite galaxies with precision requires a thorough understanding of several critical parameters. These parameters encompass precise measurements of the satellite’s position, distance, line-of-sight velocity, proper motions, the underlying gravitational potential of the host galaxy, and the Galactocentric distance of the Sun, along with its motion relative to the Galactic center. Unfortunately, many of these key parameters remain inadequately constrained, introducing a notable degree of uncertainty in orbital analyses (Bland-Hawthorn & Gerhard 2016; Joshi 2007; Schönrich et al. 2010). An essential consideration is measurement uncertainties, especially in proper motions, which can significantly affect analyses (Pawłowski 2021a). These uncertainties can be broadly classified into statistical and systematic uncertainties (Li et al. 2021). Statistical uncertainties, arising from random measurement variations, can be mitigated through statistical methods and the utilization of larger data sets. Conversely, systematic uncertainties, not stemming from random variations but rather from inherent biases in the measurement process or instruments, pose more fundamental challenges.

Maji et al. (2017) demonstrate that the Milky Way’s disk of satellites (DoS) is dynamically transient. Their orbit modeling shows that the 11 classical satellites move away from the current DoS, causing it to thicken from $c/a \sim 0.18$ (height ~ 19.6 kpc) to $c/a \sim 0.36$ (45 kpc) in 0.5 Gyr and $c/a \sim 0.42$ (64 kpc) in 1 Gyr. This evolution persists across the two tested galactic potentials: one replacing the stellar disk with a single-component Miyamoto–Nagai potential and another using only an NFW dark matter halo potential. However, Pawłowski et al. (2017) notes that Maji et al. (2017) have overlooked measurement uncertainties, such as those related to proper motions in their studies, and argues that ignoring observational biases further undermines the reliability of Maji et al. (2017)’s conclusions regarding the plane of satellite galaxies. Similarly, Sawala et al. (2023) argues that the plane of satellites is more likely transient rather than rotationally supported, because a back- and forward-integration of

Table 1. Potential Models

Potential Model	Halo Mass
MW_{low}	$4.8 \times 10^{11} M_{\odot}$
MW_{fiducial}	$8 \times 10^{11} M_{\odot}$
MW_{high}	$11.2 \times 10^{11} M_{\odot}$

satellite galaxy orbits resulted in a widening of the inferred plane thickness. However, they did not take the systematic errors in Gaia proper motions into account. These uncertainties are crucial, as they can significantly impact the measured values and potentially alter the results. Without accounting for these uncertainties, the conclusions drawn about the stability and alignment of the Milky Way's satellite plane might be overly optimistic or pessimistic. This could lead to misinterpretations about the dynamical status of these satellite structures, thereby influencing our understanding of the formation and evolution of the Milky Way and its satellite system. The incorporation of measurement uncertainties, particularly in proper motion data, is essential for achieving a more realistic and reliable understanding of the satellite galaxies' orbital behaviors. This is especially the case when studying the joint behavior of an ensemble of satellite galaxies, since errors then have the effect of washing out intrinsic correlations (and approaches such as Monte-Carlo sampling from the uncertainties effectively apply the errors twice, Pawłowski 2021a).

To address this, in this paper, we explore how different levels and types of measurement uncertainties affect the inferred stability of planes of satellite galaxies. Specifically, we employ computer simulations to model the orbital evolution of test satellite galaxies around a host galaxy that were set up as intrinsically stable satellite planes. We mock-observed these by applying controlled degrees of observational errors on their evolved positions and velocities, and then backward-integrate them to determine how well the intrinsically stable dynamical evolution can be inferred.

This paper is structured as follows. In Sect. 1 we explain the methodology. This includes setting up an artificial satellite plane, the employed plane fitting routine, the performed orbit integrations, how mock measurement errors were applied, and the subsequent backward integration of the test satellites. Our results are compiled in Sect. 3 for various combinations of measurement errors, assumed Milky Way potentials, and initial orbital eccentricity distributions. We end with a discussion and conclusions in Sect. 4.

2. Methodology

To study the evolution of artificial planes of satellite galaxies, it is essential that the test satellites are appropriately arranged around the host galaxy to initially form a planar structure. To achieve this, we are using the Milky Way and its satellite distribution as a model to establish an artificial plane of satellite galaxies. The Milky Way's satellite plane, VPOS, spans approximately 250 kpc in radius with a root mean square thickness ranging from 20 to 30 kpc. Therefore, the radial distribution, R , of N_{sat} test satellites ranges from 20 to 250 kpc, while the vertical distribution extends from 0 to 20 kpc (Pawłowski 2018, 2021b). To generate a random radial distribution, we utilize the Von Neumann rejection algorithm, also referred to as rejection sampling (Neumann 1951). This statistical technique facilitates the generation of random samples from a desired probability distribution. Fig. 1 shows the face-on and edge-on views of the randomly dis-

tributed $N_{\text{sat}} = 25$ test satellites around a host galaxy, which is initially set up as a planar structure. Here, the satellite plane is set to be perpendicular to the host galaxy's stellar disk. To produce the radial distance distribution, a power-law distribution function is used:

$$f(r) = r^{\alpha} \quad (1)$$

Here, for α , we used -3 . For the velocities, first we need the unit vectors for each test satellite in the radial, tangential, and perpendicular directions, with respect to the satellite plane. In vector representation, they can be written as:

$$\mathbf{V}_{\text{rad}; i} = |\mathbf{V}_{\text{rad}; i}| \cdot \hat{r}_i \quad (2)$$

$$\mathbf{V}_{\text{tan}; i} = |\mathbf{V}_{\text{tan}; i}| \cdot \hat{t}_i \quad (3)$$

$$\mathbf{V}_{\text{perp}; i} = |\mathbf{V}_{\text{perp}; i}| \cdot \hat{p}_i, \quad (4)$$

where, $\mathbf{V}_{\text{rad}; i}$, $\mathbf{V}_{\text{tan}; i}$, and $\mathbf{V}_{\text{perp}; i}$ represent the radial, tangential, and perpendicular velocity vectors of the i -th test satellite, respectively. $|\mathbf{V}_{\text{rad}; i}|$, $|\mathbf{V}_{\text{tan}; i}|$, and $|\mathbf{V}_{\text{perp}; i}|$ denote the magnitudes of the radial, tangential, and perpendicular velocity, respectively. \hat{r}_i , \hat{t}_i , and \hat{p}_i signify the unit vectors along the radial, tangential, and perpendicular directions for the i -th test satellite.

Hammer et al. (2021) and Cautun & Frenk (2017) investigated the relations between radial and tangential velocities of Milky Way satellite galaxies and reported a tangential bias. Specifically, Cautun & Frenk (2017) demonstrated that 9 out of 10 satellites with measured proper motions exhibit highly tangentially biased motions, with 80% or more of their orbital kinetic energy attributed to tangential motion. Given the significance of tangential velocity, we set both $|\mathbf{V}_{\text{perp}; i}|$ and $|\mathbf{V}_{\text{rad}; i}|$ to zero initially, indicating no motion in radial and perpendicular directions. This means only the tangential component is relevant. Satellites are initialized with a tangential speed equal to the MW_{fiducial} , see Table 1, gravitational potential's circular velocity, guaranteeing circular orbits. To make orbits eccentric, the tangential unit vectors of all satellites are rotated by an angle θ around the perpendicular unit vector. For each test satellite, the values for θ are drawn from a uniform distribution with some maximum range of $-\theta_{\text{max}}$ and $+\theta_{\text{max}}$, as mentioned in Table 2.

Once we have the radial $\mathbf{V}_{\text{rad}; i}$, perpendicular $\mathbf{V}_{\text{perp}; i}$, and tangential $\mathbf{V}_{\text{tan}; i}$ velocity components, we convert them into a Cartesian coordinate system. Thus, this allows us to fully describe the motion of test satellites in the simulated galaxy system.

2.1. Plane fitting

Once the test satellites are distributed around their host galaxy, the next step involves performing plane fitting to analyze the spatial arrangement of these satellites. This technique helps us understand whether the satellites are arranged in a planar structure or scattered more isotropically around the host galaxy. For this purpose, a viable method of unweighted plane-fitting technique is used Metz et al. (2007). This method commences with the calculation of the moment of inertia tensor of the satellite distribution, followed by its diagonalization. The process begins by determining the centroid, r_0 , of the data points:

$$r_0 = \frac{1}{N} \sum_{i=1}^N r_i \quad (5)$$

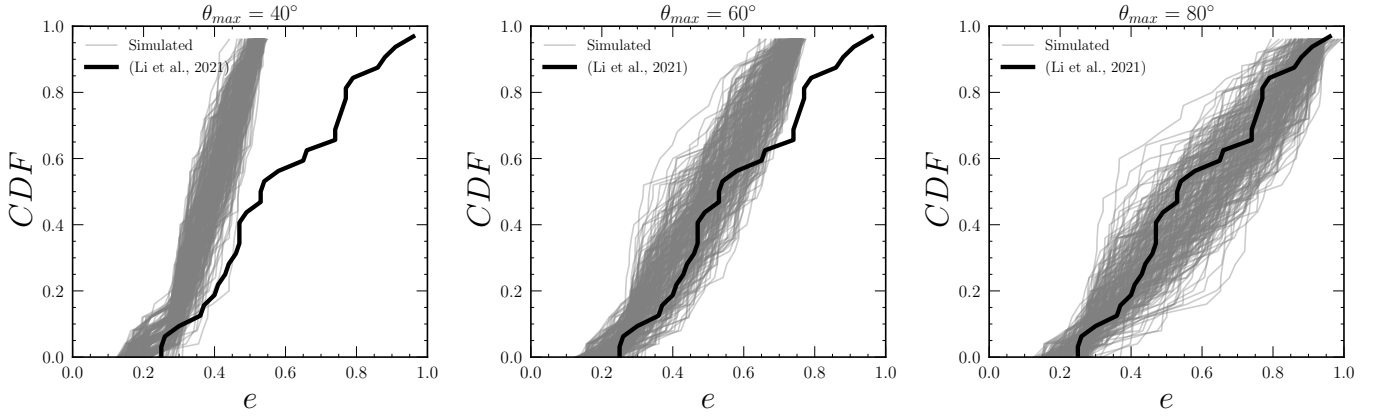


Fig. 2. Comparison of eccentricity, (e), distributions across different θ : The figure presents the eccentricity CDF for three different θ_{max} : 40° , 60° , and 80° , from left to right, respectively, as shown in gray. The predominant black line in each panel signifies observed data for the Milky Way satellites from (Li et al. 2021), while the overlaid gray CDF represent simulated results for N_{sat} test satellites.

Subsequent to this, an eigenvalue analysis of the moment of inertia tensor, \mathbf{T}_0 , is conducted for the position vectors, $\hat{\mathbf{r}}_i = \mathbf{r}_i - \mathbf{r}_0$, $i = 1 \dots n$ (Metz et al. 2007; Pawłowski et al. 2013).

$$\mathbf{T}_0 = \sum_{i=1}^N \left[(\mathbf{r}_i - \mathbf{r}_0)^2 \cdot \mathbf{1} - (\mathbf{r}_i - \mathbf{r}_0) \cdot (\mathbf{r}_i - \mathbf{r}_0)^T \right] \quad (6)$$

Here $\mathbf{1}$ denotes the unit matrix and \mathbf{r}^T is the transposed version of the vector \mathbf{r} . The square root of the eigenvalues of the moment of inertia indicates the extent along three axes (a , b , c) of the fitted ellipsoid to the satellite distribution. These values are proportional to the rms deviation relative to the eigenvectors of \mathbf{T} . The eigenvector corresponding to the largest eigenvalue defines the normal of the plane, encompassing the centroid. Meanwhile, the eigenvectors corresponding to the intermediate and smallest eigenvalues indicate the directions of the intermediate and major axes of the distribution, respectively. Consequently, the axial ratios c/a and b/a are determined. A small value of c/a suggests two possibilities: if b/a is large, it indicates an oblate distribution resembling a thin plane; if b/a is similarly small ($c/a \approx b/a$), it suggests a narrow prolate distribution resembling a filament-like shape (Metz et al. 2007).

2.2. Adopted Potential

Understanding the gravitational potential and mass distribution of the Milky Way is crucial for numerically integrating the orbits of test satellites. Despite extensive research over the past century, the exact distribution of the Milky Way's mass remains a topic of debate. Current estimates of the total mass of the Milky Way range between $0.5 - 3 \times 10^{12} M_\odot$ (Wang et al. 2020), varying based on the methodology and underlying assumptions (Bland-Hawthorn & Gerhard 2016). Therefore, significant uncertainty surrounds the mass of the Milky Way, necessitating the consideration of these ambiguities in mass distribution.

For this study, we use one fiducial potential for the forward integration, and three distinct gravitational potentials, as detailed in Table 1, to investigate their effects on the evolution and inferred stability of the Plane of Satellite Galaxies in backward integration. This is to evaluate what effect adopting an incorrect Milky Way mass has on the inferred satellite plane's evolution. To numerically integrate orbits, we rely on Galpy (Bovy 2015) to investigate the orbital properties of the test satellites.

Within the `galpy.potential` module, there exists a model named `MWPotential2014`, which represents the Milky Way's gravitational potential and is obtained by fitting to a wide range of observational data. This is a simplified static potential model, which is composed of the following components:

A spherically symmetric power-law density potential with an exponential cut-off for the bulge:

$$\rho(r) = \rho_0 r^{-\alpha} \exp\left(-\left(\frac{r}{r_c}\right)^2\right), \quad (7)$$

with a power-law index of $\alpha = 1.8$, and a cut-off radius of $r_c = 1.9$ kpc.

The disk component is modeled using the axisymmetric Miyamoto–Nagai disk (Miyamoto & Nagai 1975):

$$\Phi(R, z) = -\frac{\Phi_0}{\sqrt{R^2 + (a + \sqrt{z^2 + b^2})^2}}, \quad (8)$$

where $a = 3$ kpc and $b = 0.28$ kpc.

The dark matter halo is characterized by the Navarro–Frenk–White (NFW) halo (Navarro 1996):

$$\rho(r) = \frac{\rho_0}{(r/h)(1+r/h)^2}, \quad (9)$$

with a characteristic radius $h = 16$ kpc.

`MWPotential2014` is scaled such that the circular velocity at a distance of 8 kpc from the galactic center within the disc ($z = 0$ kpc) is 220 km/s with a virial mass of about $8 \times 10^{11} M_\odot$. In this study, we refer to this potential as the Fiducial Potential, MW_{fiducial} . For the remaining two Milky Way potentials, MW_{fiducial} is adjusted by re-scaling the halo mass to achieve the desired mass distribution. Specifically, the MW_{low} model is configured with a halo mass 40% less than that of MW_{fiducial} , while MW_{high} has a halo mass 40% greater than that of MW_{fiducial} , thus providing deeper insights into the influence of mismatching the Milky Way's mass on the inferred behavior and stability of satellite galaxy planes.

2.3. Forward Integration

We conduct forward integration of the satellite system over a span of 5 Gyr for $N = 20$ random realizations of the initial setups. We select three distinct maximum tangential velocity angles θ_{\max}

Table 2. Parameters for forward integration models.

Model	N_{sat}	θ_{max}	Potential Model	$N_{\text{realization}}$
FI-01	25	40°	MW_{fiducial}	20
FI-02	25	60°	MW_{fiducial}	20
FI-03	25	80°	MW_{fiducial}	20

Notes. The table lists the model numbers (FI), the number of satellites (N_{sat}), the maximum angle θ_{max} in degrees, the gravitational potential model (MW_{fiducial}), and the number of realizations ($N_{\text{realization}}$) for each forward integration scenario.

$= 40^\circ, 60^\circ$, and 80° , for the forward integration as shown in Table 2. It is worth noting that the larger the angle, the more eccentric orbits are possible.

The resulting cumulative distribution functions (CDFs) of eccentricity for the three different θ values are illustrated in Fig. 2. Furthermore, we overlay as a solid black curve the eccentricity data for the observed Milky Way satellites from (Li et al. 2021) onto the plot, which contains the data of 46 satellite galaxies from Fritz et al. (2018), McConnachie & Venn (2020) and Simon (2019). However, for our comparison, we picked 35 satellite galaxies, as 11 of them had an eccentricity $e \gg 1$. This addition allows us to compare the simulated eccentricities with those of observed Milky Way satellite galaxies. From the comparison, it becomes apparent that $\theta_{\text{max}} = 80^\circ$ closely aligns with the observed eccentricities of satellite galaxies. Each forward integration was conducted utilizing the MW_{fiducial} potential model. Fig. 2 also shows that the range of CDF for Li et al. (2021) spans approximately 0.2 to 1.0. For the simulated eccentricity of our initial test runs, the range is between 0.0 and 1.0, because circular orbits were also included. To align the simulated eccentricity of orbits with the observed data, values ranging between $\theta = -20^\circ$ and 20° were excluded to ensure that no perfectly circular orbits are generated.

2.4. Uncertainties

To determine the motion of a satellite galaxy precisely, its position, distance and 3D motion are crucial. Spectroscopy is used to track the motion of a galaxy using the Doppler effect. However, it is essential to note that radial velocity measures only one dimension. To determine how a galaxy moves tangentially across the sky, proper motions are measured. The Hubble Space Telescope (HST) has measured the proper motion of most of the 11 brightest, classical satellite galaxies of the Milky Way (Redd 2018). Since then, largely due to the advent of Gaia, the availability of proper motion information has significantly improved (Gaia Collaboration et al. 2016b,a). However, highly accurate proper motion measurements remain limited and are available only for the more massive and luminous or nearby satellite galaxies.

According to Gaia DR2, the random proper motion errors for Milky Way satellites range approximately between 0.006 and 0.641 mas yr^{-1} (Fritz et al. 2018), and the corresponding systematic errors are estimated to be approximately 0.035 to 0.066 mas yr^{-1} (Gaia Collaboration et al. 2018a,b). In Gaia EDR3, the uncertainties in proper motions, derived from both statistical and systematic errors, have approximately halved (Lindegren et al. 2021; McConnachie & Venn 2020; Li et al. 2021; Battaglia et al. 2022).

In this study, we investigate four different ranges of proper motion uncertainties: $\epsilon_\mu = 0.00 \text{ mas yr}^{-1}$, 0.04 mas yr^{-1} , 0.08 mas yr^{-1} , and 0.12 mas yr^{-1} . We specifically opted for 0.00

mas yr^{-1} proper motion uncertainties to represent cases where proper motion is measured with the highest accuracy. This condition allows us to examine the evolution of the plane of satellite galaxies under various parameters independent of proper motion errors. We randomly sample these proper motion uncertainties from Gaussian distributions with width ϵ_μ .

For distance uncertainties, we chose two specific values: $\epsilon_{\text{dist}} = 0\%$ and 5% . Distances are crucial factors in understanding the spatial distribution and dynamics of satellite galaxies around the Milky Way, and their effects on the inferred stability of the plane of satellite galaxies. Again, distance errors were sampled from a Gaussian with width ϵ_{dist} .

2.5. Backward Integration

After completing the forward integration, the orbital parameters – such as right ascension, declination, proper motion in right ascension and declination, distance, and line-of-sight velocity – are recorded for each test satellite system at the final snapshot of all simulation realizations. They are then mocked-observed by adding uncertainties in proper motions and distance, such that:

$$\mu_{\alpha^* \text{new}} = \mu_{\alpha^*} + \epsilon_\mu \quad (10)$$

$$\mu_{\delta \text{new}} = \mu_\delta + \epsilon_\mu \quad (11)$$

$$\text{dist}_{\text{new}} = \text{dist} + \epsilon_{\text{dist}} \quad (12)$$

Equation (10) – (12) provides the updated proper motions and distance parameters for each test satellite, incorporating their respective uncertainties. For the values of ϵ_μ , we draw them from a Gaussian distribution. In contrast, for ϵ_{dist} , a percentage error is drawn from a Gaussian distribution, such that more distant satellites have larger absolute distance uncertainties. Table A.1 details the ranges of uncertainties in these parameters. After performing mock observations, the system is integrated backward for 5 Gyr. This process is repeated 30 times for each of the 20 forward integrations, using different randomly generated errors each time, resulting in a total of 600 backward integrations to return the test satellite system to its initial state. This procedure is conducted using all three Milky Way potential models. Each row in Table A.1 represents a combination of various parameters that could influence the inferred stability of the satellite plane. Overall, with four proper motion uncertainties, two distance uncertainties, and three potential models, there are 24 model combinations for each θ_{max} . Each model undergoes 600 backward integrations, amounting to a total of 43,200 backward integrations.

3. Results

In this section we present the main results from the simulation¹. For brevity, and since it is the case most closely resembling the eccentricities of the observed Milky Way satellite galaxies, we only show results for $\theta_{\text{max}} = 80^\circ$. We refer the reader to Appendix A for results for the other θ_{max} , which are qualitatively similar.

3.1. Effect of Proper Motions Uncertainties

Fig. 3 presents the results focusing on introducing artificial proper motion and distance uncertainties to the test satellite system before backward integrating. These results are divided into

¹ GitHub Repository of the code used to generate the results: [Plane of Satellite Galaxies](#)

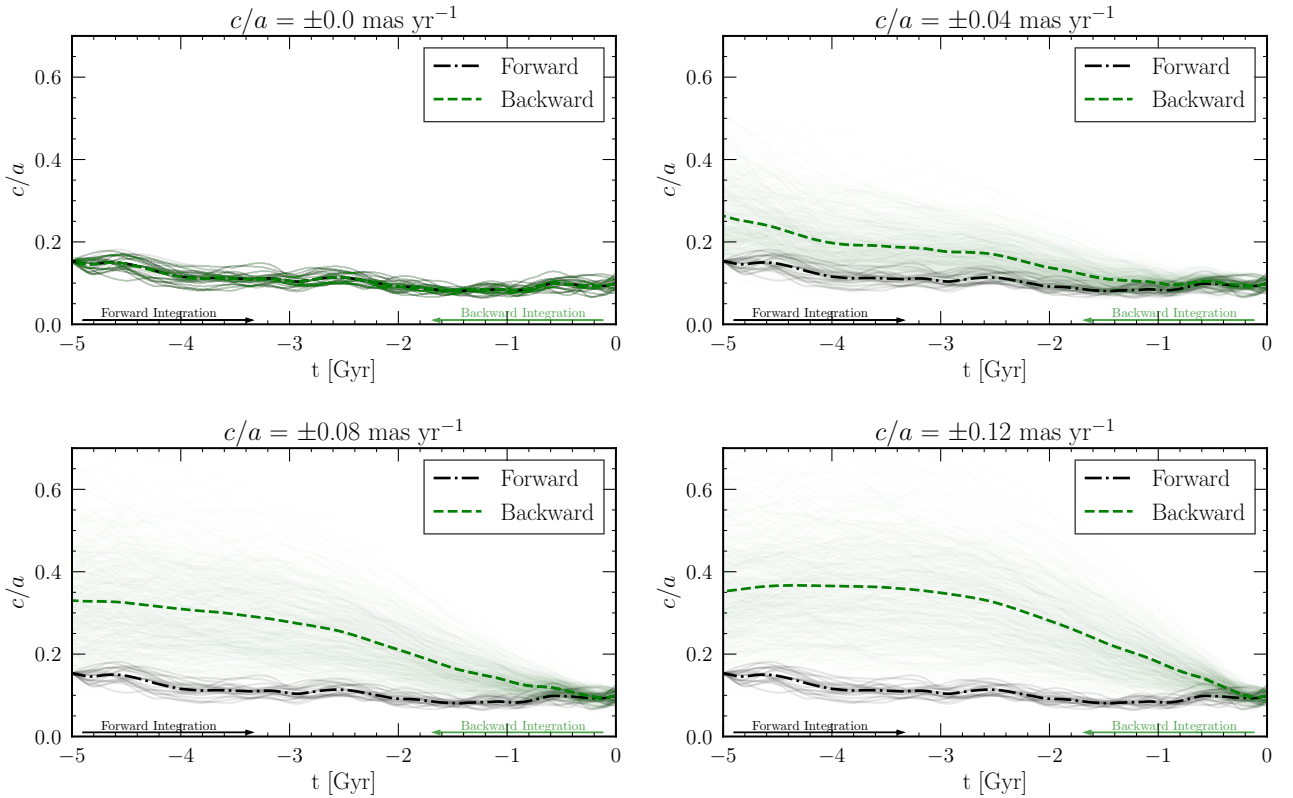


Fig. 3. Effect of proper motion uncertainties on the plane of satellite galaxies. Each panel shows $N_{\text{realization}}$ forward integrations as black curves with the mean indicated by a dot-dashed line, and $M_{\text{realization}}$ backward integrations as green curves, also with the mean indicated by a dashed line.

four panels, each corresponding to a distinct level of proper motion uncertainty.

In each panel, there is a scatter of curves shown in both gray and green, indicating the $N_{\text{realization}}$ and $M_{\text{realization}}$ numbers for forward and backward integration, respectively. The average value at each time step is shown as a dashed-dotted curve, with arrows pointing to the right and left. In this case, we use MW_{fiducial} for both forward and backward integration, and we don't add uncertainties in distance. In the upper left panel, when $\epsilon_\mu = 0.00 \text{ mas yr}^{-1}$, the mean minor-to-major ratio, c/a obtained from backward integration aligns perfectly well with the mean minor-to-major ratio, c/a obtained from the forward integration, as each forward integration curve is over-plotted by the backward integration. This shows a high degree of predictability and confirms that the orbital plane remains stable and unaltered in scenarios where the proper motion is measured with perfect accuracy. It also implies that, at least in the theoretical framework of the simulation, the inherent dynamics of the satellite system are deterministic enough to allow for precise backtracking of its orbital path when initial conditions are precisely known. These results serve as a control scenario against which the other panels, which include some amount of proper motion errors. Model BI-01 from Table A.1 shows similar behavior that, even after 3 Gyr of backward integration, the difference between forward and backward, $\Delta_{c/a} = 0.0$, and fractional change, $f_{c/a}$, is 1.00, meaning that both forward and backward integration yield the same output when proper motion uncertainties remain at zero.

In the upper right panel, we have Gaia level of systematic uncertainties, $\epsilon_\mu = 0.04 \text{ mas yr}^{-1}$. Here, a slight uncertainty in proper motion leads to a visible divergence between the mean axial ratios of forward and backward integrations. The mean axial ratio from the backward integration does not align as closely

with the forward integration as it did in the first case, when there were no uncertainties. This suggests a decrease in the predictability and inferred stability of the orbital plane with the introduction of proper motion errors. However, the curve here seems to have retained its shape to some degree. The effect of uncertainties is also evident from Model BI-02 in Table A.1, which shows that with the introduction of $\epsilon_\mu = 0.04 \text{ mas yr}^{-1}$, $\Delta_{c/a}$ shifts from 0.00 to 0.073, and $f_{c/a}$ becomes 1.69. Thus, the inferred past plane width is typically 70% higher than the true one.

Now, increasing the proper motion uncertainties to 0.08 mas yr^{-1} further diverges the means of backward and forward integration, as shown in the lower left panel. This indicates a further decline in the predictability and stability of the orbital plane as proper motion uncertainty increases. Moreover, Table A.1 also validates that in Model BI-03, $\Delta_{c/a}$ shifts yet again from 0.07 to 0.17, and $f_{c/a}$ rises to 2.64, meaning the typical inferred plane width is almost three times larger than the true one.

Furthermore, under extreme proper motion uncertainties, 0.12 mas yr^{-1} , the divergence between the mean forward and mean backward integration, shown by the dashed curves, is the most pronounced. The mean axial ratio from backward integration shows a significant divergence from the forward integration mean, implying a severe reduction in the orbital plane's predictability and stability with the highest proper motion uncertainty examined.

Moreover, the original shape of the curve is no longer discernible and deviates significantly more from the forward integration curve compared to the other uncertainties examined. This suggests that the system's actual past evolution cannot be reliably traced under such high uncertainties. It shows that the inferred dynamics of the system are highly sensitive to proper

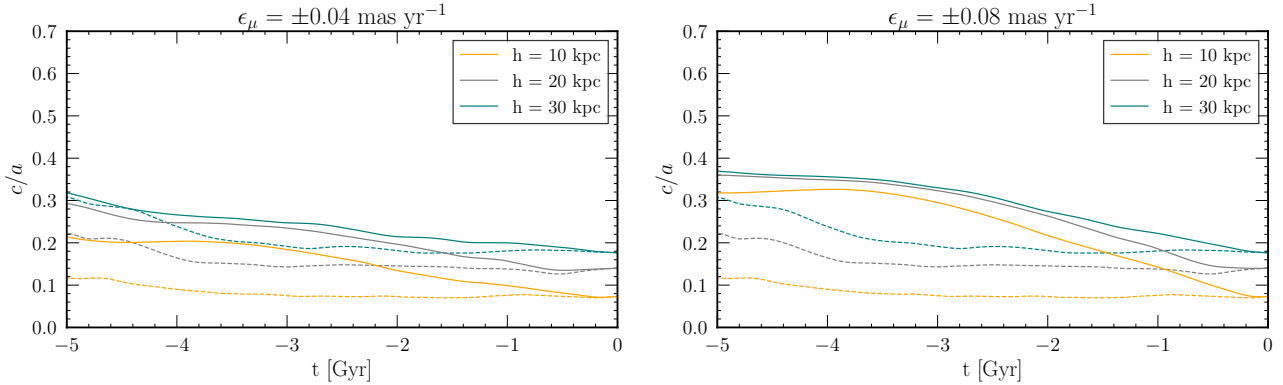


Fig. 4. Effect of proper motion uncertainties on satellite galaxies under different initial vertical distributions of $h = 10$, $h = 20$ kpc and $h = 30$ kpc. The left panel shows proper motion uncertainties of 0.04 mas yr^{-1} , while the right panel displays uncertainties of 0.08 mas yr^{-1} . Dashed curves indicate forward integration, and solid curves represent backward integration.

motion uncertainties, making it challenging to draw reliable conclusions about the satellite’s orbital evolution under these conditions. This case is represented by Model BI-04 of Table A.1; it shows that $\Delta_{c/a} = 0.24$ and $f_{c/a} = 3.32$.

3.2. Effect of Intrinsic Plane Height

We also tested whether the effect of proper motion uncertainties on the plane of satellite galaxies is sensitive to our choice of the initial vertical distribution of the intrinsic satellite planes. Specifically, we ran the system with three different plane heights — $h = 10$ kpc, $h = 20$ kpc, and $h = 30$ kpc — bracketing the range of observationally inferred satellite plane heights for the Milky Way and M31 (Ibata et al. 2013; Pawlowski et al. 2013).

Fig. 4 displays two panels showing the results for adopted proper motion uncertainties of 0.04 mas yr^{-1} and 0.08 mas yr^{-1} . In both plots, the dotted-dashed curves represent mean axis ratios of the forward integrations for the different heights of $h = 10$, 20 , and 30 kpc, indicated by orange, gray, and cyan colors, respectively. As expected, when the vertical distribution is lower, the mean axis ratio of the system is lower, making the system flatter compared to the other values of h . In the backward integration, after adding uncertainties in proper motion, we observe that all three curves exhibit a similar trend: errors in proper motion lead to an apparent widening of the satellite plane. This effect is substantial in all three cases, indicating that our findings are not sensitive to the exact choice of intrinsic plane height.

Table 3 summarizes the quantitative impact of proper motion uncertainties on the inferred change in the mean axis ratio. For a smaller intrinsic plane height of $h = 10$ kpc (model BI-L10 and BI-H10 in Table 3), the relative effect is stronger, with $f_{c/a} = 2.45$ (3.94) compared to $f_{c/a} = 1.64$ (2.25) for the model of $h = 20$ kpc for adopted proper motion uncertainties of 0.04 (0.08) mas yr^{-1} . Similarly, for an intrinsically wider plane (model BI-L30 and BI-H30 in Table 3), the relative change in plane flattening is a bit lower, with $f_{c/a} = 1.29$ and 1.72 for proper motion uncertainties of 0.04 and 0.08 mas yr^{-1} , respectively. However, the absolute change in axis ratio, measured via $\Delta_{c/a}$, does not differ as much.

3.3. Effect of Distance Uncertainties

We now go one step further and additionally introduce 5% distance uncertainties before backwards-integrating, to study the behavior of the plane under both proper motions and distance

uncertainties. In all four panels of Fig. 5, backward integration now has two curves: one without distance uncertainties (shown in green) and one with 5% distance uncertainties (shown in red). As shown in the upper left panel of Fig. 5, when proper motion uncertainties are ignored, there is a noticeable effect of distance uncertainties; the system does not return to its original state but instead experiences a slight change. Despite this, there is still decent agreement between the mean backward and forward integrations in axis ratio, suggesting that the inferred fundamental orbital evolution is not drastically impacted, even with the introduction of 5% uncertainties in the distances of the test satellites. It is also evident from Table A.1 where in models BI-01 and B1-13, both $\Delta_{c/a}$ and $f_{c/a}$ have changed just slightly from 0.00 to 0.02 and 1.00 to 1.17 respectively after 3 Gyr of backward integration. A 5% error in the distances thus translates to a widening of the inferred past plane height over the true one, reaching up to 17% at specific times (e.g., after 3 Gyr), although the deviation remains negligible for the majority of the 5 Gyr integration period.

As we introduce proper motion uncertainties, we observe that the relative effect of distance uncertainties fades away as the proper motion error becomes dominant. This is evident in the bottom-right panel of Fig. 5, where the highest proper motion uncertainties result in both curves showing similar behavior. Moreover, although not included in this paper, a test for 10% distance uncertainties was also performed. We found that the effect on the system becomes more pronounced with increasing uncertainties. However, this effect diminishes as the uncertainties in proper motions increase.

We also conducted additional tests where we examined the correlation between proper motion errors and distance errors. We found that although there is a noticeable change, the overall effect is not extreme. This is discussed in Appendix B.1.

Table 3. Parameters and results for backward integration models at 3 Gyr for different intrinsic plane height, similar to Table A.1.

Model	$\epsilon_\mu [\text{mas yr}^{-1}]$	$h [\text{kpc}]$	$\Delta_{c/a}$	$f_{c/a}$
BI-L10	± 0.04	10	0.10 ± 0.06	2.45 ± 0.84
BI-L20	± 0.04	20	0.09 ± 0.07	1.64 ± 0.51
BI-L30	± 0.04	30	0.06 ± 0.06	1.29 ± 0.32
BI-H10	± 0.08	10	0.19 ± 0.09	3.94 ± 1.32
BI-H20	± 0.08	20	0.18 ± 0.09	2.25 ± 0.75
BI-H30	± 0.08	30	0.14 ± 0.09	1.72 ± 0.49

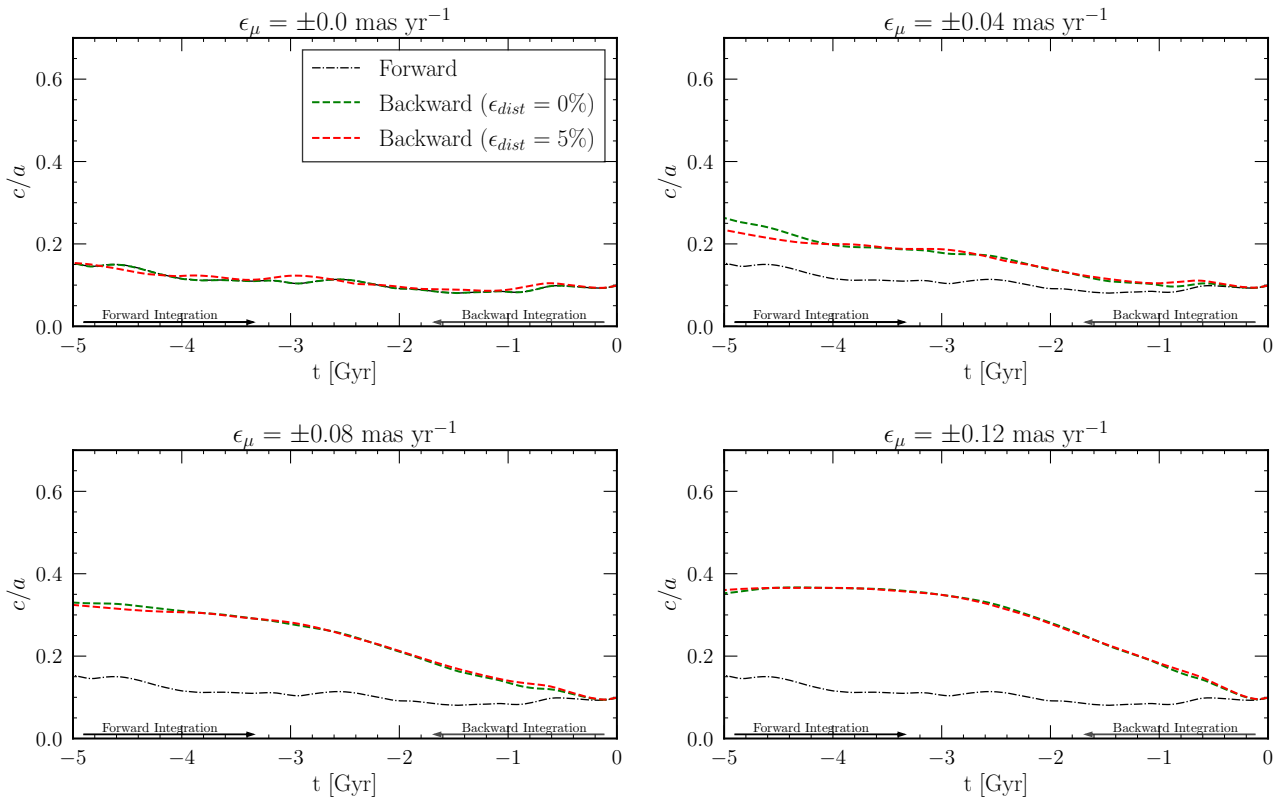


Fig. 5. Similar to Fig. 3, but here we compare it with 5% distance uncertainties in the system as well. The green curve in each panel shows 0% distance uncertainties, whereas the red curve shows 5% distance uncertainties. The uncertainties in proper motions are as follows: 0.00 mas yr^{-1} in the upper left panel, 0.04 mas yr^{-1} in the upper right panel, 0.08 mas yr^{-1} in the lower left panel, and 0.12 mas yr^{-1} in the lower right panel. Both forward and backward integrations are done using the MW_{fiducial} potential model.

3.4. Effect of Adopted Potential

In the upper left panel of Fig. 6, without the uncertainties in proper motion and distance, the results provide a clear picture of the satellite plane's fundamental dynamical behavior when subjected to different potential models. The colored curves depict the mean backward integration under different Milky Way potentials. The backward integration, particularly the green curve representing the MW_{fiducial} potential, demonstrates perfect consistency with its forward counterpart, implying a stable evolution when the potential model is the same. This case is already discussed in the previous sections.

The red curve, representing the MW_{high} model, exhibits a reasonable degree of stability, although it does not completely resemble the forward integration, suggesting some sensitivity to the host galaxy's mass assumptions. This difference is shown in BI-09 of Table A.1, which shows $\Delta_{c/a} = 0.01$ after 3 Gyr, and $f_{c/a} = 1.13$. In contrast, the blue curve, representing the MW_{low} mass model, shows a completely different behavior from the other models. Its axis ratio initially increases before flattening, which could imply a dynamical history distinct from the correct one for the plane of satellites within such a lower-mass potential model. Here, for lower-mass Milky Way potential, $\Delta_{c/a} = 0.03$ after 3 Gyr, and $f_{c/a} = 1.27$.

The other three panels of Fig. 6 show the effect of both potential models and proper motion uncertainties on the stability of the plane of satellites. In the upper right panel, we have proper motion uncertainties of $\pm 0.04 \text{ mas yr}^{-1}$. The effect under MW_{fiducial} has already been discussed in the previous section. For the MW_{high} model, it generally follows a similar trend to MW_{fiducial} , but with slightly larger axis ratio values. Whereas,

the MW_{low} again shows a distinct behavior where it initially rises and then flattens out over time.

When adding more uncertainties, up to Gaia levels and even with some extremes, the effect strengthens further in all the remaining panels, and the plane of the system becomes even wider. Under 0.12 mas yr^{-1} proper motion uncertainty, all three systems seem to have a similar trend, suggesting that higher proper motion uncertainties overshadow the effect of using an incorrect Milky Way model. This observation indicates that, at higher levels of proper motion uncertainty, the distinctions between the various Milky Way potential models become less pronounced, as the increased uncertainty tends to dominate the inferred dynamics of the satellite plane.

Building upon this, we add one more layer: distance uncertainties. By comparing Fig. 6 and Fig. 7, we can again see a noticeable effect of distance uncertainties on the system under all three potential models, but it does not change the evolution of the plane drastically. However, in the presence of higher proper motion uncertainties, the effect of distance uncertainties is again overshadowed under all three potential models. Models BI-13 to BI-24 show this behavior when 5% of uncertainties were induced.

We also checked that our results remain qualitatively unchanged when using different Milky Way gravitational potentials. Specifically, we performed the analysis with `MilkyWayPotential2022` from `Galaxy` (Price-Whelan 2017), including variations in halo mass and proper motion uncertainties, and found no substantial differences in the overall trends; see Appendix B.2.

3.5. Analysis of Individual Axes

The behavior of the minor-to-major axial ratio in the MW_{low} potential model differs from other models, warranting a closer examination of how the extent of the test satellite system changes along its different axes, from major to minor. Fig. 8 illustrates the influence of proper motion uncertainties on the mean values of the three axes: a (major axis), b (intermediate axis), and c (minor axis). The influence of proper motion uncertainties is presented row-wise, while the axes are displayed column-wise in the figure. Each panel further shows curves in three colors, depicting the impact of potential models. The solid curves represent the results when $\epsilon_{\text{dist}} = 0\%$, while the dashed-dotted curves indicate the results when $\epsilon_{\text{dist}} = 5\%$. The first row shows $\pm 0.00 \text{ mas yr}^{-1}$ proper motion uncertainties and 0% distance uncertainties. Here, both MW_{fiducial} and MW_{high} show similar behavior under respective axes, with and without distance uncertainties. Over time, the axes tend to decrease, particularly under MW_{high} potential model. In contrast, MW_{low} demonstrates a completely different and opposite behavior. Over time, in backward integration, all the axes under MW_{low} tend to increase.

In these models, the variations in axis lengths are a direct consequence of changes in gravitational pull due to mass differences. In the MW_{high} model, with increased halo mass, all axes become more compact as the structure becomes more gravitationally bound. Conversely, in the MW_{low} model, a reduction in mass leads to an elongation of the axes, particularly in a and b . This suggests that in the MW_{low} model, more satellites become unbound, causing them to drift away from their host galaxies. It is important to note that the MW_{fiducial} model was used as a baseline for the MW_{high} and MW_{low} models, with the halo mass

being adjusted by 40% (increased and decreased, respectively). However, the response of the axis extents to these adjustments is striking, with the Milky Way potential with 40% less halo mass having a more pronounced effect on the system than the one with a 40% higher halo mass. Moreover, with the inclusion of distance errors, each axis in every potential model extends slightly, indicating a noticeable, though not extreme, effect on the orbital axes.

We additionally tested and recalculated the c/a ratio by excluding test satellites beyond 300 kpc and only considering those within this threshold, as discussed in Appendix B.3. We find that this does not result in any major influence.

3.6. Inferred Escaping Satellites

Fig. 9 shows the average number of test satellites that surpass a distance of 300 kpc from the galactic center under proper motion uncertainties and various potential models. This plot is divided into four panels, and each panel further shows curves in three colors, depicting the impact of potential models. The solid curves represent the results when $\epsilon_{\text{dist}} = 0\%$, while the dashed-dotted curves indicate the results when $\epsilon_{\text{dist}} = 5\%$. In the upper left panel, when there are no proper motion uncertainties, for MW_{low} , the curve initially shows a relatively stable number of satellites that go beyond 300 kpc in backward integration, with and without distance uncertainties. Over time, the number gradually increases before reaching a plateau. This outcome is expected, as reducing the halo mass by 40% lowers the gravitational binding force, allowing more satellites to become unbound and drift beyond 300 kpc.

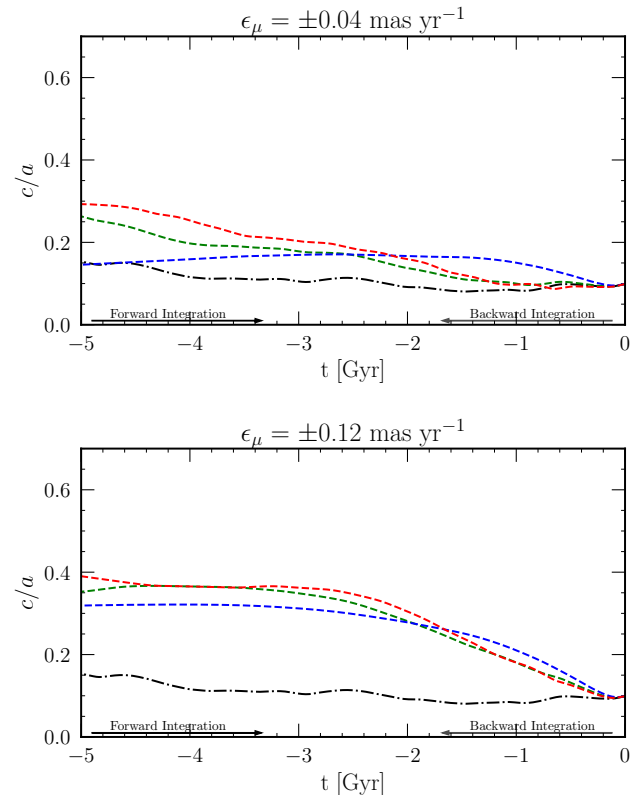
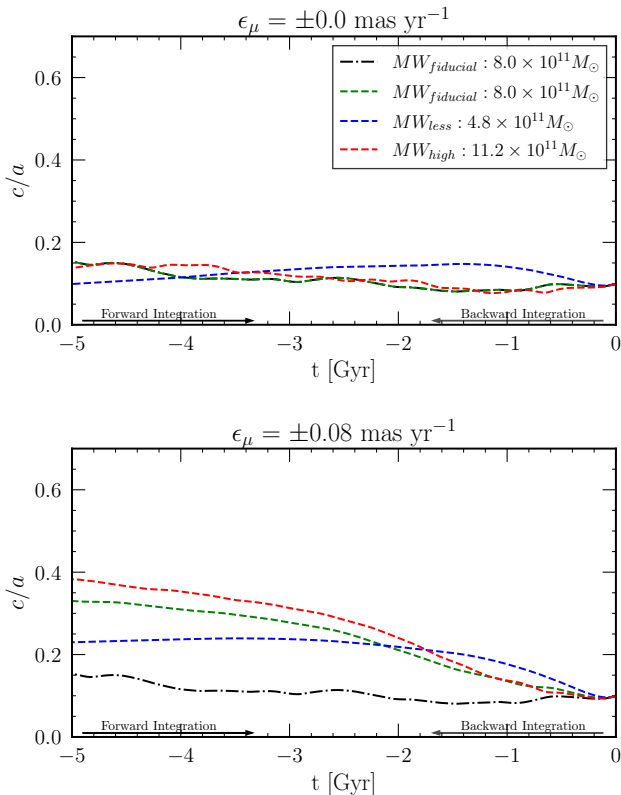


Fig. 6. Evolution of the plane of satellite galaxies with proper motion uncertainties included in each panel. The black dashed-dotted curves represent the mean axis ratio for forward integration, while the colored dashed curves indicate the mean axis ratio for backward integration under different potential models characterized by halo mass. Specifically, the blue, green, and red dashed curves correspond to the c/a values under the MW_{low} , MW_{fiducial} , and MW_{high} potential models, respectively. Note that these results do not account for distance uncertainties.

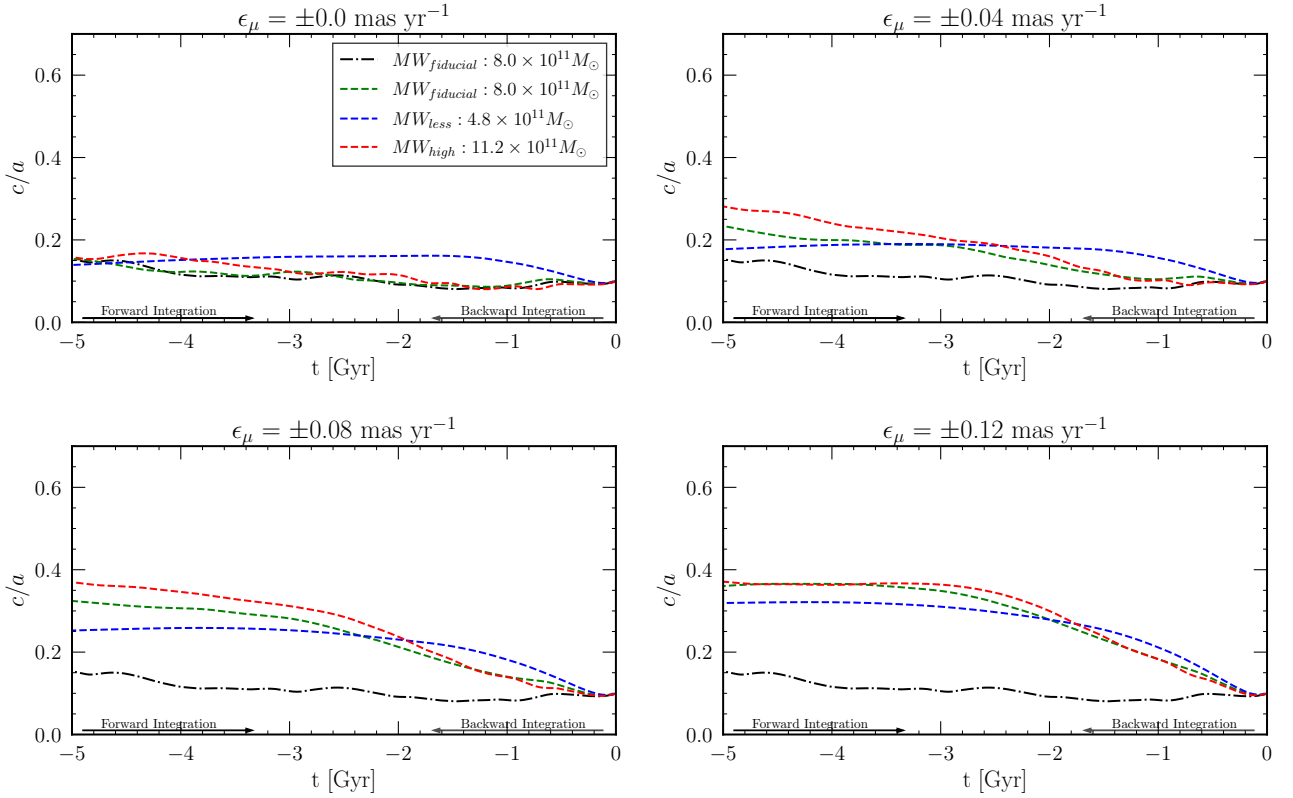


Fig. 7. Similar to 6, but here we include a 5% uncertainty in distances.

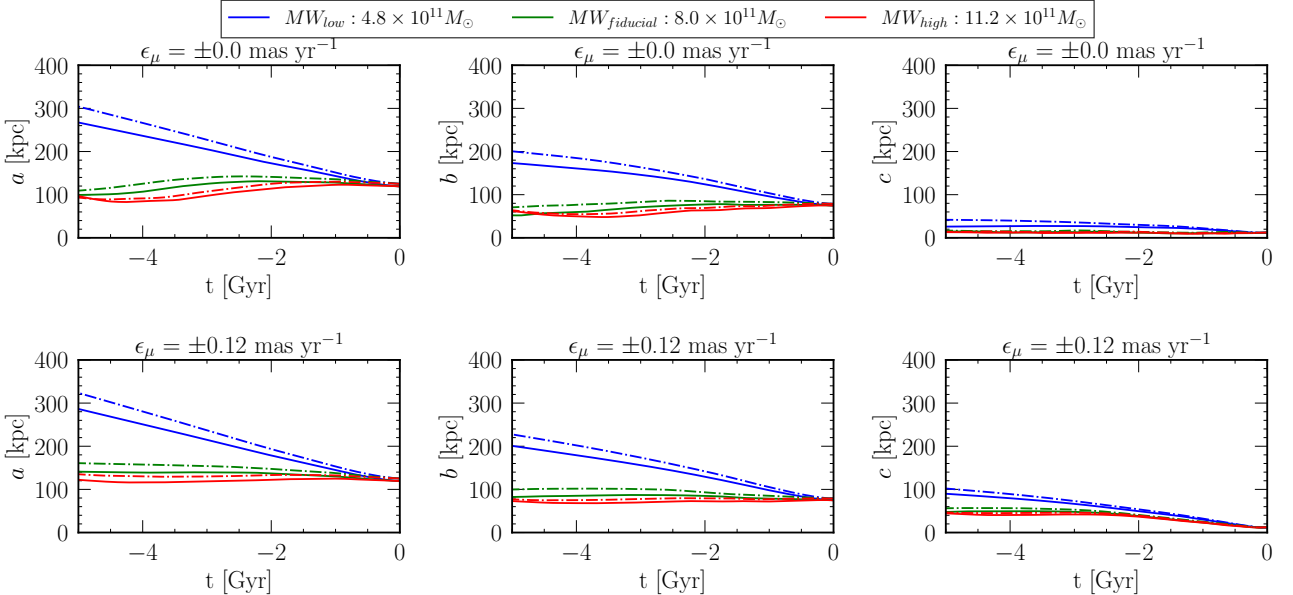


Fig. 8. Comparative analysis of galactic orbital axes under proper motion uncertainties and different potential models at $\theta_{tan} = 80^\circ$. It shows the mean values of 600 major, minor, and intermediate axes calculated through backward integration. Each panel represents a unique combination of proper motion uncertainty and potential models. Dotted-dashed curves show the effect of distance uncertainties, while solid curves ignore it. The rows correspond to different levels of proper motion uncertainty, while the columns represent the three axes: major (first column), intermediate (second column), and minor (third column).

Unlike MW_{low} model, the other two potential models show an opposite behavior. In $MW_{fiducial}$, the number of test satellites going beyond 300 kpc decreases over time, and at 5 Gyr, all N_{sat} test satellites remain under the 300 kpc limit. This trend is even more pronounced in the MW_{high} potential model, where the number of distant test satellites progressively diminishes over time

due to the higher halo mass. Furthermore, the other three panels demonstrate the effect of proper motion uncertainties on satellite dynamics, showing that as uncertainties increase, more test satellites remain at distances greater than 300 kpc across all models. Proper motion errors affect this on average by preferentially in-

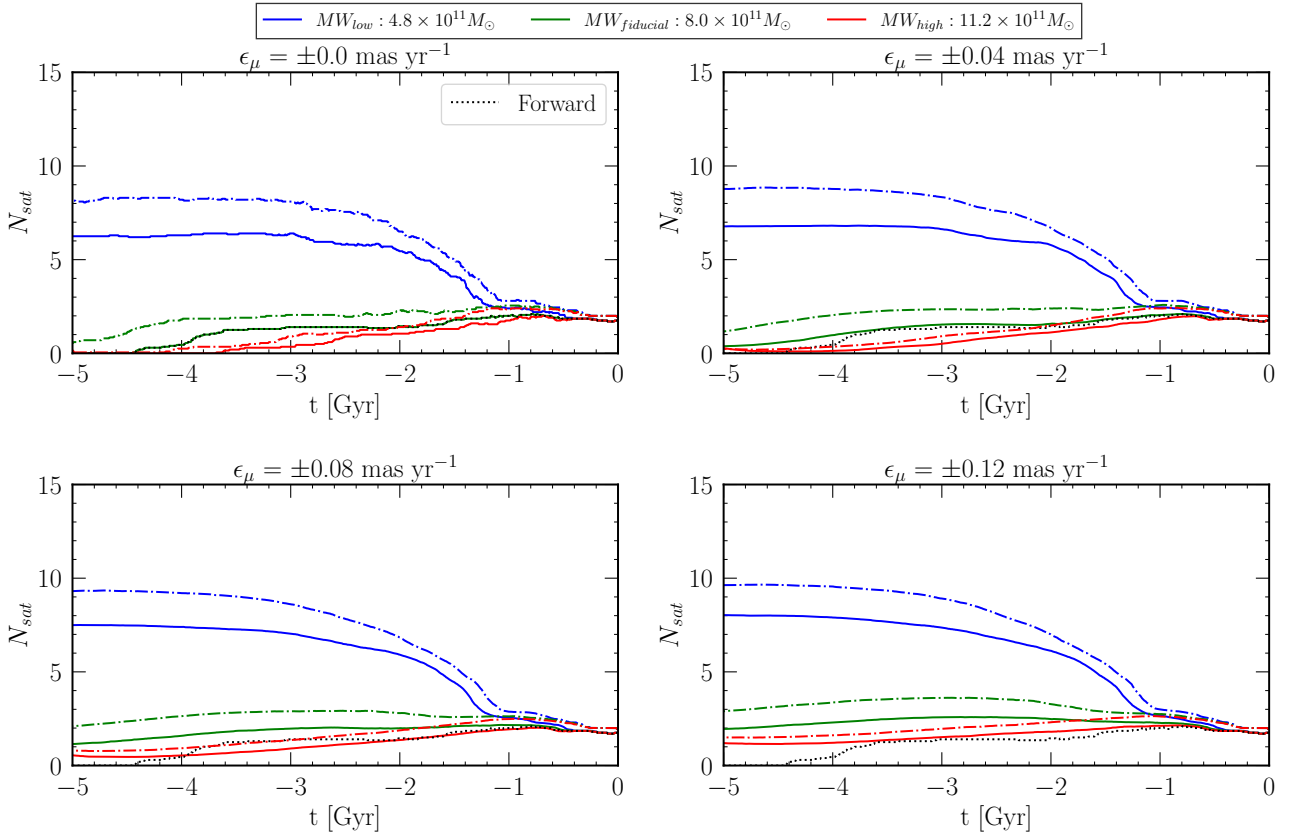


Fig. 9. Average number of test satellite exceeding 300 kpc of radial distance under proper motion uncertainties. The four panels represent different level of proper motion uncertainties. Each panel shows six curves, which visualize the number of test satellites residing beyond 300 kpc of distance under three different potential models. Here dotted-dashed curves show the results when including distance uncertainties, while solid line ignore distance uncertainties and only consider the proper motion errors.

creasing the inferred velocities and thus the energies of satellites, effectively ejecting more test satellites.

Furthermore, when comparing the curves with and without distance uncertainties, we observe a clear effect of these uncertainties, which further increases the number of test satellites that exceed the 300 kpc range. In Table A.1, the column $N_{\text{sat}} > 300$ kpc represents models BI-05 to BI-08 without induced distance errors in MW_{low} , and models BI-17 to BI-20 with distance errors. From this, it is evident that the inclusion of distance errors at 3 Gyr leads to a greater inferred loss of satellites in the system.

4. Conclusion and Outlook

We have investigated the impact of different types of measurement uncertainties on the *inferred* stability of artificial, intrinsically stable planes of satellite galaxies. Our key results are:

- When the test satellite galaxies' proper motions are measured with perfect accuracy (or $\epsilon_\mu = 0.00 \text{ mas yr}^{-1}$) and no other errors are introduced, we infer that the system remains highly stable.
- At the level of minimum Gaia uncertainties (with $\epsilon_\mu = 0.04 \text{ mas yr}^{-1}$, similar to Gaia systematics), the inferred plane widths begin to diverge from true one towards larger values. While the thin initial plane remains relatively well constrained, its inferred width relative to the true plane almost doubles within 3 Gyr. As we increase the applied proper motion uncertainties ($\epsilon_\mu = 0.08$ and 0.12 mas yr^{-1}), the inferred plane widths increase substantially, and one might infer that

the intrinsically stable satellite planes are highly unstable. The c/a shows a linear increase with the addition of more uncertainties.

- When performing backward integration with three different intrinsic plane height ($h = 10, 20, \text{ and } 30 \text{ kpc}$), we find that applying realistic uncertainties in the proper motion introduce a substantial broadening in the plane of satellites in all cases. The apparent broadening effect we identified is therefore not sensitive to the exact intrinsic plane height assumed for the plane.
- When applying 5% distance uncertainties, a noticeable effect is observed which increases the plane width during backward-integration relative to the intrinsic planes' width. However, this does not dominate the inferred evolution of the satellite plane. Additionally, the impact of distance uncertainties becomes less important with higher levels of proper motion uncertainties.
- The influence of adopting incorrect Milky Way potential models leads to an apparent widening of the inferred past satellite planes. The impact is especially significant for MW_{low} , which has a 40% smaller halo mass compared to the fiducial model considered for our intrinsic satellite planes. Due to its lower mass, it struggles to maintain cohesion among the test satellites, leading to increased radial distances and an extension of its major, minor, and intermediate axes. However, under larger proper motion uncertainties, the influence of adopting incorrect Milky Way potential models diminishes, as the system deviates from its true configuration across all potential models.

Thus, this study emphasizes the necessity of precise determination of proper motion, distances of satellite galaxies, and the Milky Way's gravitational potential. We have seen how variations in these quantities can significantly shift our inference of the evolution of intrinsically stable satellite planes, especially in proper motion and halo mass of the host galaxy. We argue that underestimating the halo mass would also lead one to infer that more satellites escape from the host (and might thus appear unbound) than is the case in the true fiducial model.

Accurate measurement of the Milky Way potential is thus vital for a comprehensive study of its satellite system and for broader insights into galactic evolution and interactions. We also found that the results are not very sensitive to the choice of the number of integrations; in our study, 600 backward integrations per model were sufficient.

However, it is crucial to acknowledge certain limitations in this research. A significant caveat is the absence of consideration for the gravitational effects of massive satellite galaxies like the LMC. These celestial bodies, owing to their substantial mass, could affect the mass estimates of the Milky Way galaxy (Erkal et al. 2020), and exert significant gravitational forces that can profoundly influence the Milky Way and its surroundings (Garavito-Camargo et al. 2021; Pawłowski et al. 2022; Vasiliev 2023), and thus can influence the stability of the satellite plane. The omission of these influences in the current study represents a notable limitation in our analysis. Additionally, this study assumes a spherical dark matter halo; however, it's important to acknowledge that the halo could be triaxial (Law et al. 2009), which might have implications for our findings.

Future studies could enhance our understanding by incorporating the gravitational influence of massive satellite galaxies like the LMC and SMC, as well as considering different shapes of the dark matter halo. Such an approach would allow for a more comprehensive analysis of the satellite plane's dynamics, taking into account the complexities of real-world scenarios. Additionally, in this study, we assume a static dark matter halo over the 5 Gyr integration period. However, this simplification overlooks important evolutionary effects. Over time, the halo mass is expected to grow as it accretes dark matter, with a smaller mass in the past and a larger mass in the future. This impacts satellite orbits, particularly at larger radii. Pace et al. (2022) focuses on observations and finds that the orbital computations of 46 dwarf spheroidal galaxies (dSphs) using a static Milky Way potential reveal that, while pericenter and apocenter distances can be derived, the inclusion of the LMC's potential alters these parameters by more than 25% for 40% of the sample. Similar studies have also been conducted using cosmological simulations D'Souza & Bell (2022); Santistevan et al. (2024). Additionally, the influence of the baryonic disk leads to adiabatic contraction, increasing the dark matter density at smaller radii, which affects the inner orbits of satellites (Cautun et al. 2020). Generally, however, such additional dynamical effects can be expected to increase the uncertainty in past satellite trajectories, as we have only limited constraints on their exact implementation. We therefore expect them to exacerbate the trend of inferring less stable satellite plane dynamics when backward-integrating. Moreover, an important dynamical process that is not included in our model is dynamical friction. This effect, especially for massive satellites orbiting within a host potential, can lead to the gradual decay of orbits as they lose energy and angular momentum to the dark matter background (Esquivel & Fuchs 2007; Ogiya & Burkert 2016; Taylor & Babul 2001). Over time, this process can significantly alter satellite trajectories and contribute to the disruption of coherent planar structures.

Our method can be extended to examine the observed planes of satellites of M31, Cen A and others. However, the application to these systems requires careful consideration of observational uncertainties, such as proper motions, distances, and gravitational potentials, which are significantly higher compared to our current analysis (in the case of M31) or thus far inaccessible (for more distant systems). Additionally, apart from these observational limitations, the evolution of such planes would also be sensitive to the initial distribution of the positions and velocities of the test satellites. Variations in the initial conditions could lead to notable differences in the structure and persistence of the planes over time. By accounting for these factors, our approach can provide valuable insights into the dynamics of satellite galaxies in diverse environments, further broadening the scope of our findings.

Our numerical experiments demonstrate how intrinsically stable, co-orbiting planes of satellite galaxies display a significant increase in their plane height if they are backward-integrated after applying measurement errors. This is already the case for errors in proper motion comparable to the current Gaia systematics of ~ 0.033 mas yr^{-1} (Lindegren et al. 2021; McConnachie & Venn 2020; Li et al. 2021). Such an increase in plane height was argued by Sawala et al. (2023) as indicative that the Milky Way's Vast Polar Structure is more likely a transient rather than a rotationally supported feature and thus consistent with ΛCDM expectations. Similar arguments were put forward earlier by Maji et al. (2017) based on earlier, less accurate proper motion measurements. In their studies, the authors integrated the orbits of observed Milky Way satellite galaxies in a static potential, akin to our numerical experiments, and measured the time evolution of the inferred thickness of plane fits. However, our work shows that such an increasing thickness does *not* necessarily imply an absence of a kinematically coherent, dynamically stable, or long-lived satellite plane. In the case of an underlying, intrinsically stable satellite plane, realistic measurement errors alone, as well as assuming a mismatching Galactic potential, can already cause apparent thickening. Furthermore, one needs to be cautious in how errors are applied. Given that, for example, the measured most-likely proper motions of observed satellite galaxies are already subject to measurement error, sampling the errors in a Monte-Carlo fashion (as e.g. done in Sawala et al. 2023) then effectively applies these errors twice. For our study, this means that our applied proper motion error on the level of $\epsilon_\mu = 0.04$ mas yr^{-1} corresponds to a case of Monte-Carlo sampling of orbits based on observed data with a measurement error of $\epsilon_\mu/\sqrt{2} = 0.028$ mas yr^{-1} . Monte-Carlo sampling thus further enhances the effect we have identified in our study of artificially increasing the inferred satellite plane height when backward-integrating, because it typically adds more dispersion to an ensemble of satellites. Merely finding an increase in the inferred plane height of an observed satellite structure under orbit integration – without accounting for the impact of measurement errors (especially in proper motions) or mismatches in the assumed Galactic gravitational potential – is thus insufficient to claim that the structure is not dynamically stable or transient, or that it is therefore consistent with ΛCDM .

Acknowledgements. MSP acknowledges funding via a Leibniz-Junior Research Group (project number J94/2020). Moreover, this work made use of the following software packages: `astropy` (Astropy Collaboration et al. 2013, 2018, 2022), `matplotlib` (Hunter 2007), `numpy` (Harris et al. 2020), `python` (Van Rossum et al. 1995), `scipy` (Virtanen et al. 2020; Gommers et al. 2025), and `galpy` (Bovy 2015). Software citation information aggregated using `The Software Citation Station` (Wagg & Broekgaarden 2024; Wagg et al. 2024).

References

Ade, P. A., Aghanim, N., Arnaud, M., et al. 2016, *A&A*, 594, A13

Ahmed, S. H., Brooks, A. M., & Christensen, C. R. 2017, *MNRAS*, 466, 3119

Astropy Collaboration, Price-Whelan, A. M., Lim, P. L., et al. 2022, *ApJ*, 935, 167

Astropy Collaboration, Price-Whelan, A. M., Sipőcz, B. M., et al. 2018, *ApJ*, 156, 123

Astropy Collaboration, Robitaille, T. P., Tollerud, E. J., et al. 2013, *A&A*, 558, A33

Banik, I., Thies, I., Truelove, R., et al. 2022, *MNRAS*, 513, 129

Battaglia, G., Taibi, S., Thomas, G. F., & Fritz, T. K. 2022, *A&A*, 657, A54

Bland-Hawthorn, J., & Gerhard, O. 2016, *ARA&A*, 54, 529

Bovy, J. 2015, *ApJS*, 216, 29

Casetti-Dinescu, D. I., Pawłowski, M. S., Girard, T. M., et al. 2024, arXiv e-prints, arXiv:2409.08252

Cautun, M., Benítez-Llambay, A., Deason, A. J., et al. 2020, *MNRAS*, 494, 4291

Cautun, M., & Frenk, C. S. 2017, *MNRAS*, 468, L41

Conn, A. R., Lewis, G. F., Ibata, R. A., et al. 2013, *ApJ*, 766, 120

D’Onghia, E., & Lake, G. 2008, *ApJ*, 686, L61

D’Souza, R., & Bell, E. F. 2022, *MNRAS*, 512, 739

Erkal, D., Belokurov, V. A., & Parkin, D. L. 2020, *MNRAS*, 498, 5574

Esquivel, O., & Fuchs, B. 2007, *MNRAS*, 378, 1191

Fouquet, S., Hammer, F., Yang, Y., Puech, M., & Flores, H. 2012, *MNRAS*, 427, 1769

Fritz, T. K., Battaglia, G., Pawłowski, M. S., et al. 2018, *A&A*, 619, A103

Gaia Collaboration, Brown, A. G. A., Vallenari, A., et al. 2018a, *A&A*, 616, A1

Gaia Collaboration, Brown, A. G. A., Vallenari, A., et al. 2016a, *A&A*, 595, A2

Gaia Collaboration, Helmi, A., van Leeuwen, F., et al. 2018b, *A&A*, 616, A12

Gaia Collaboration, Prusti, T., de Bruijne, J. H. J., et al. 2016b, *A&A*, 595, A1

Garavito-Camargo, N., Patel, E., Besla, G., et al. 2021, *ApJ*, 923, 140

Gommers, R., Virtanen, P., Haberland, M., et al. 2025, *scipy/scipy: SciPy 1.15.2*

Hammer, F., Wang, J., Pawłowski, M. S., et al. 2021, *ApJ*, 922, 93

Harris, C. R., Millman, K. J., van der Walt, S. J., et al. 2020, *Nature*, 585, 357

Hunter, J. D. 2007, *Computing in Science & Engineering*, 9, 90

Ibata, R. A., Gilmore, G., & Irwin, M. J. 1994, *Nature*, 370, 194

Ibata, R. A., Lewis, G. F., Conn, A. R., et al. 2013, *Nature*, 493, 62

Joshi, Y. C. 2007, *MNRAS*, 378, 768

Júlio, M. P., Pawłowski, M. S., Tony Sohn, S., et al. 2024, *A&A*, 687, A212

Kanehisa, K. J., Pawłowski, M. S., & Müller, O. 2023a, *MNRAS*, 524, 952

Kanehisa, K. J., Pawłowski, M. S., Müller, O., & Sohn, S. T. 2023b, *MNRAS*, 519, 6184

Karachentsev, I. D. & Kroupa, P. 2024, *MNRAS*, 528, 2805

Kroupa, P., Theis, C., & Boily, C. M. 2005, *A&A*, 431, 517

Law, D. R., Majewski, S. R., & Johnston, K. V. 2009, *ApJ*, 703, L67

Li, H., Hammer, F., Babusiaux, C., et al. 2021, *ApJ*, 916, 8

Li, Y.-S., & Helmi, A. 2008, *MNRAS*, 385, 1365

Libeskind, N. I., Knebe, A., Hoffman, Y., et al. 2011, *MNRAS*, 411, 1525

Lindgren, L., Klioner, S. A., Hernández, J., et al. 2021, *A&A*, 649, A2

Lovell, M. R., Eke, V. R., Frenk, C. S., & Jenkins, A. 2011, *MNRAS*, 413, 3013

Lynden-Bell, D. 1976, *MNRAS*, 174, 695

Maji, M., Zhu, Q., Marinacci, F., & Li, Y. 2017, *ApJ*, 843, 62

McConnachie, A. W. & Venn, K. A. 2020, *Research Notes of the American Astronomical Society*, 4, 229

Metz, M., Kroupa, P., & Jerjen, H. 2007, *MNRAS*, 374, 1125

Metz, M., Kroupa, P., & Libeskind, N. I. 2008, *ApJ*, 680, 287

Metz, M., Kroupa, P., Theis, C., Hensler, G., & Jerjen, H. 2009, *ApJ*, 697, 269

Miyamoto, M., & Nagai, R. 1975, *PASJ*, 27, 533

Müller, O., Pawłowski, M. S., Jerjen, H., & Lelli, F. 2018, *Science*, 359, 534

Müller, O., Pawłowski, M. S., Lelli, F., et al. 2021, *A&A*, 645, L5

Navarro, J. 1996, in *IAU Symposium*, Vol. 171, *New Light on Galaxy Evolution*, ed. R. Bender & R. L. Davies, 255

Neumann, V. 1951, *Notes by GE Forsythe*, 36

Ogiya, G. & Burkert, A. 2016, *MNRAS*, 457, 2164

Pace, A. B., Erkal, D., & Li, T. S. 2022, *ApJ*, 940, 136

Pawłowski, M. S. 2018, *Modern Physics Letters A*, 33, 1830004

Pawłowski, M. S. 2021a, *Nature Astronomy*, 5, 1185

Pawłowski, M. S. 2021b, *Galaxies*, 9, 66

Pawłowski, M. S., Bullock, J. S., Kelley, T., & Famaey, B. 2019, *ApJ*, 875, 105

Pawłowski, M. S., Dabringhausen, J., Famaey, B., et al. 2017, *Astronomische Nachrichten*, 338, 854

Pawłowski, M. S., Famaey, B., Merritt, D., & Kroupa, P. 2015, *ApJ*, 815, 19

Pawłowski, M. S., Kroupa, P., & de Boer, K. S. 2011, *A&A*, 532, A118

Pawłowski, M. S., Kroupa, P., & Jerjen, H. 2013, *MNRAS*, 435, 1928

Pawłowski, M. S., Müller, O., Taibi, S., et al. 2024, *A&A*, 688, A153

Pawłowski, M. S., Oria, P.-A., Taibi, S., Famaey, B., & Ibata, R. 2022, *ApJ*, 932, 70

Pawłowski, M. S., Pflamm-Altenburg, J., & Kroupa, P. 2012, *MNRAS*, 423, 1109

Pawłowski, M. S. & Tony Sohn, S. 2021, *ApJ*, 923, 42

Peacock, J. A., Cole, S., Norberg, P., et al. 2001, *Nature*, 410, 169

Price-Whelan, A. M. 2017, *The Journal of Open Source Software*, 2, 388

Redd, N. T. 2018, 115, 12836

Riess, A. G., Filippenko, A. V., Challis, P., et al. 1998, *AJ*, 116, 1009

Santistevan, I. B., Wetzel, A., Tollerud, E., et al. 2024, *MNRAS*, 527, 8841

Sawala, T., Cautun, M., Frenk, C., et al. 2023, *Nature Astronomy*, 7, 481

Schönrich, R., Binney, J., & Dehnen, W. 2010, *MNRAS*, 403, 1829

Shao, S., Cautun, M., Frenk, C. S., et al. 2018, *MNRAS*, 476, 1796

Shapley, H. 1938, *Nature*, 142, 715

Simon, J. D. 2019, *ARA&A*, 57, 375

Smith, R., Duc, P. A., Bournaud, F., & Yi, S. K. 2016, *ApJ*, 818, 11

Sohn, S. T., Patel, E., Fardal, M. A., et al. 2020, *ApJ*, 901, 43

Spergel, D. N., Verde, L., Peiris, H. V., et al. 2003, *ApJS*, 148, 175

Taibi, S., Pawłowski, M. S., Khoperskov, S., Steinmetz, M., & Libeskind, N. I. 2024, *A&A*, 681, A73

Taylor, J. E. & Babul, A. 2001, *ApJ*, 559, 716

Tegmark, M., Blanton, M. R., Strauss, M. A., et al. 2004, *ApJ*, 606, 702

Tully, R. B., Libeskind, N. I., Karachentsev, I. D., et al. 2015, *ApJ*, 802, L25

Van Rossum, G., Drake, F. L., et al. 1995, *Python reference manual*, Vol. 111 (Centrum voor Wiskunde en Informatica Amsterdam)

Vasiliev, E. 2023, *Galaxies*, 11, 59

Virtanen, P., Gommers, R., Oliphant, T. E., et al. 2020, *Nature Methods*, 17, 261

von Humboldt, A. & Otte, E. C., eds. 1997, *Cosmos: a sketch of the physical description of the universe*

Wagg, T., Broekgaarden, F., & Gültekin, K. 2024, *TomWagg/software-citation-station: v1.2*

Wagg, T. & Broekgaarden, F. S. 2024, arXiv e-prints, arXiv:2406.04405

Wang, J., Frenk, C. S., & Cooper, A. P. 2013, *MNRAS*, 429, 1502

Wang, W., Han, J., Cautun, M., Li, Z., & Ishigaki, M. N. 2020, *Science China Physics, Mechanics, and Astronomy*, 63, 109801

Appendix A: Analysis at $\theta_{\max} = 40^\circ$ and 60°

This appendix presents the simulations involving less eccentric orbits. Results and analysis for $\theta_{\tan} = 80\%$ have been discussed in detail in Section 3. Following a similar pattern, we here present the results which are obtained for $\theta_{\tan} = 40^\circ$ and 60° .

Fig. B.1 and A.2 display results analogous to those in Section 3. These scenarios exhibit qualitatively comparable patterns. The figures are segmented into four panels, each representing different levels of proper motion uncertainties. The mean c/a ratios for forward integration are depicted with black curves, whereas those for backward integration are shown in colored curves. Similar to the previously discussed case, it becomes increasingly difficult to accurately determine the stability of the satellite plane as the level of proper motion errors escalates. Furthermore, in these results too, the behavior of the system under MW_{low} is different from the other two potential models.

Fig. 2 shows that as θ_{\max} increases, the orbits become more eccentric, and this effect is clearly observed when we consider the results under θ_{\max} . By comparing the results at $\theta_{\max} = 40\%, 60\%, 80\%$, as shown in Tables A.2, A.3, and A.1, we see that at a given level of proper motion uncertainty, the satellite plane widens more for larger θ_{\max} . For instance, in Model BI-02, when $\epsilon_\mu = 0.04 \text{ mas yr}^{-1}$, $\Delta_{c/a}$ is 0.04, 0.06, and 0.07 for $\theta_{\tan} = 40\%, 60\%, 80\%$, respectively, and increases gradually. Furthermore, the influence of eccentric orbits is also apparent when comparing the curves in Fig. B.1, A.2, and 6. In cases with

less eccentric orbits ($\theta_{\tan} = 40\%$), the plane appears relatively smoother and flatter. In contrast, as the orbits become more eccentric, the evolution of the plane flattening becomes increasingly irregular and pronounced, indicating a significant impact of orbital eccentricity on the satellite's dynamics. This suggests that as θ_{\max} increases, not only does the eccentricity of the orbits intensify, but the overall structure and stability of the orbital plane are also affected, leading to a more complex and varied orbital configuration.

Similarly, Fig. A.1 and A.3 display the effects of distance uncertainties on the test satellite system for $\theta_{\tan} = 40^\circ$ and 60° , respectively. The analysis, as discussed in Section 3, indicates that the inclusion of distance errors has a noticeable effect on the c/a . However, this does not significantly impact the overall evolution of c/a .

Finally, similar to Fig. 9, here Fig. A.4 and A.5 display the number of test satellites that exceeded the 300 kpc radius threshold under $\theta_{\max} = 40^\circ$ and 60° , respectively. The effect of proper motion errors is depicted in each of the four panels, with each line within a panel representing the influence of different Milky Way potential models. Dotted-dashed curves show the effect of 5% distance uncertainties, while solid curves show 0% distance uncertainties. The influence of eccentricities is clearly apparent in these figures. For a given model, less eccentric orbits result in fewer test satellites escaping the system compared to those with higher eccentricities. This trend is further corroborated by the data presented in Tables A.1, A.2, and A.3. In these tables, un-

Table A.1. Parameters and results for backward integration models at 3 Gyr in backward integration with $\theta_{\max} = 80^\circ$.

Model	ϵ_μ [mas yr^{-1}]	ϵ_{dist} [%]	Potential Forward	Potential Backward	$M_{\text{realization}}$	$\Delta_{c/a}$	$f_{c/a}$	$N_{\text{sat}}(> 300 \text{ kpc})$
BI-01	± 0.00	0	MW_{fiducial}	MW_{fiducial}	600	0.00 ± 0.01	1.00 ± 0.12	1.40 ± 0.92
BI-02	± 0.04	0	MW_{fiducial}	MW_{fiducial}	600	0.07 ± 0.05	1.69 ± 0.51	1.53 ± 1.01
BI-03	± 0.08	0	MW_{fiducial}	MW_{fiducial}	600	0.17 ± 0.09	2.64 ± 0.87	1.97 ± 1.10
BI-04	± 0.12	0	MW_{fiducial}	MW_{fiducial}	600	0.24 ± 0.11	3.32 ± 1.07	2.57 ± 1.14
BI-05	± 0.00	0	MW_{fiducial}	MW_{low}	600	0.03 ± 0.05	1.27 ± 0.44	6.40 ± 1.50
BI-06	± 0.04	0	MW_{fiducial}	MW_{low}	600	0.06 ± 0.05	1.61 ± 0.47	6.63 ± 1.46
BI-07	± 0.08	0	MW_{fiducial}	MW_{low}	600	0.13 ± 0.07	2.26 ± 0.68	7.03 ± 1.38
BI-08	± 0.12	0	MW_{fiducial}	MW_{low}	600	0.21 ± 0.10	2.97 ± 0.93	7.36 ± 1.43
BI-09	± 0.00	0	MW_{fiducial}	MW_{high}	600	0.01 ± 0.02	1.13 ± 0.16	0.35 ± 0.48
BI-10	± 0.04	0	MW_{fiducial}	MW_{high}	600	0.10 ± 0.06	1.93 ± 0.58	0.51 ± 0.59
BI-11	± 0.08	0	MW_{fiducial}	MW_{high}	600	0.21 ± 0.10	2.98 ± 0.97	0.91 ± 0.79
BI-12	± 0.12	0	MW_{fiducial}	MW_{high}	600	0.26 ± 0.11	3.45 ± 1.02	1.51 ± 0.93
BI-13	± 0.00	5	MW_{fiducial}	MW_{fiducial}	600	0.02 ± 0.02	1.17 ± 0.18	2.05 ± 1.07
BI-14	± 0.04	5	MW_{fiducial}	MW_{fiducial}	600	0.08 ± 0.05	1.78 ± 0.51	2.35 ± 1.12
BI-15	± 0.08	5	MW_{fiducial}	MW_{fiducial}	600	0.18 ± 0.09	2.68 ± 0.86	2.90 ± 1.14
BI-16	± 0.12	5	MW_{fiducial}	MW_{fiducial}	600	0.24 ± 0.11	3.32 ± 1.06	3.61 ± 1.17
BI-17	± 0.00	5	MW_{fiducial}	MW_{low}	600	0.05 ± 0.06	1.51 ± 0.57	8.10 ± 1.58
BI-18	± 0.04	5	MW_{fiducial}	MW_{low}	600	0.08 ± 0.06	1.80 ± 0.57	8.34 ± 1.52
BI-19	± 0.08	5	MW_{fiducial}	MW_{low}	600	0.15 ± 0.08	2.41 ± 0.71	8.61 ± 1.53
BI-20	± 0.12	5	MW_{fiducial}	MW_{low}	600	0.21 ± 0.08	2.95 ± 0.79	8.92 ± 1.54
BI-21	± 0.00	5	MW_{fiducial}	MW_{high}	600	0.02 ± 0.02	1.16 ± 0.21	0.90 ± 0.77
BI-22	± 0.04	5	MW_{fiducial}	MW_{high}	600	0.10 ± 0.06	1.94 ± 0.61	0.92 ± 0.74
BI-23	± 0.08	5	MW_{fiducial}	MW_{high}	600	0.21 ± 0.10	2.97 ± 0.97	1.36 ± 0.91
BI-24	± 0.12	5	MW_{fiducial}	MW_{high}	600	0.26 ± 0.11	3.46 ± 1.05	1.97 ± 1.02

Notes. The table lists the model numbers (BI), proper motion errors (ϵ_μ) in milliarcseconds per year, distance errors (ϵ_{dist}) in percentage, the gravitational potential used for forward and backward integration (MW_{fiducial} , MW_{low} , MW_{high}), the number of realizations $M_{\text{realization}}$ for each backward integration, the average absolute difference in average minor-to-major axis ratio flattening between forward and backward integration ($\Delta_{c/a}$), and the average relative change in this quantity between the forward and backward integration ($f_{c/a}$) along with their standard deviations (std) as a measure of their spread between different realizations at 3 Gyr. Additionally, $N_{\text{sat}} > 300 \text{ kpc}$ denotes the absolute number of satellite realizations beyond 300 kpc with their standard deviations.

der all models, the column representing the number of satellites with distances greater than 300 kpc ($N_{\text{sat}} > 300$ kpc) consistently increases as the eccentricity of the orbits increases.

Appendix B: Additional checks

Apart from the main results, we also checked some additional checks to see the behavior of the satellite plane.

Appendix B.1: Correlated PM and Dist errors

We also test whether a correlation between proper motion and distance errors affects the inferred evolution of the satellite plane, as fainter test satellites could have both larger proper motion and distance uncertainties. To investigate this, we performed an additional analysis, comparing two cases (see Fig. B.2): one with a proper motion (PM) error of 0.04 mas/yr and a 10% distance error, and another with a PM error of 0.1 mas/yr and a 10% distance error. Each plot includes two backward integrations—one with a PM-distance error correlation and one without. In both cases, the same errors are used, but in the 'correlated' case, the errors are ranked and assigned to the test satellites such that satellites farther away have progressively larger distance and proper motion errors. We find that the effect is not extreme but leads to an increase in the inferred widening of the satellite plane. This suggests that the approach of using uncorrelated errors is conservative and at most underestimates the impact of uncertainties. Moreover, as expected, with higher PM error, the effect becomes more pronounced, aligning with what we observed in our main results.

Table A.2. Parameters and results for backward integration models at 3 Gyr in backward integration, similar to Table A.1 but at $\theta_{\text{max}} = 40^\circ$.

Model	ϵ_μ [mas yr $^{-1}$]	ϵ_{dist} [%]	Potential		M _{realization}	$\Delta_{c/a}$	$f_{c/a}$	$N_{\text{sat}}(> 300 \text{ kpc})$
			Forward	Backward				
BI-01	± 0.00	0	<i>MW</i> _{fiducial}	<i>MW</i> _{fiducial}	600	0.00 ± 0.02	1.00 ± 0.18	0.50 ± 0.59
BI-02	± 0.04	0	<i>MW</i> _{fiducial}	<i>MW</i> _{fiducial}	600	0.04 ± 0.04	1.37 ± 0.34	0.63 ± 0.72
BI-03	± 0.08	0	<i>MW</i> _{fiducial}	<i>MW</i> _{fiducial}	600	0.12 ± 0.08	2.07 ± 0.69	1.17 ± 0.94
BI-04	± 0.12	0	<i>MW</i> _{fiducial}	<i>MW</i> _{fiducial}	600	0.20 ± 0.12	2.75 ± 1.04	1.80 ± 1.15
BI-05	± 0.00	0	<i>MW</i> _{fiducial}	<i>MW</i> _{low}	600	0.02 ± 0.03	1.13 ± 0.28	4.35 ± 1.82
BI-06	± 0.04	0	<i>MW</i> _{fiducial}	<i>MW</i> _{low}	600	0.05 ± 0.04	1.43 ± 0.35	4.69 ± 1.65
BI-07	± 0.08	0	<i>MW</i> _{fiducial}	<i>MW</i> _{low}	600	0.11 ± 0.07	1.99 ± 0.59	5.29 ± 1.61
BI-08	± 0.12	0	<i>MW</i> _{fiducial}	<i>MW</i> _{low}	600	0.18 ± 0.10	2.58 ± 0.84	5.80 ± 1.67
BI-09	± 0.00	0	<i>MW</i> _{fiducial}	<i>MW</i> _{high}	600	0.01 ± 0.02	1.11 ± 0.16	0.00 ± 0.00
BI-10	± 0.04	0	<i>MW</i> _{fiducial}	<i>MW</i> _{high}	600	0.05 ± 0.04	1.43 ± 0.31	0.12 ± 0.33
BI-11	± 0.08	0	<i>MW</i> _{fiducial}	<i>MW</i> _{high}	600	0.13 ± 0.08	2.16 ± 0.72	0.43 ± 0.61
BI-12	± 0.12	0	<i>MW</i> _{fiducial}	<i>MW</i> _{high}	600	0.21 ± 0.11	2.83 ± 0.10	1.01 ± 0.88
BI-13	± 0.00	5	<i>MW</i> _{fiducial}	<i>MW</i> _{fiducial}	600	0.01 ± 0.02	1.12 ± 0.145	0.75 ± 0.83
BI-14	± 0.04	5	<i>MW</i> _{fiducial}	<i>MW</i> _{fiducial}	600	0.06 ± 0.04	1.51 ± 0.37	0.97 ± 0.85
BI-15	± 0.08	5	<i>MW</i> _{fiducial}	<i>MW</i> _{fiducial}	600	0.14 ± 0.08	2.21 ± 0.73	1.67 ± 1.05
BI-16	± 0.12	5	<i>MW</i> _{fiducial}	<i>MW</i> _{fiducial}	600	0.21 ± 0.11	2.81 ± 0.93	2.31 ± 1.24
BI-17	± 0.00	5	<i>MW</i> _{fiducial}	<i>MW</i> _{low}	600	0.04 ± 0.04	1.31 ± 0.36	5.80 ± 2.18
BI-18	± 0.04	5	<i>MW</i> _{fiducial}	<i>MW</i> _{low}	600	0.06 ± 0.04	1.57 ± 0.39	6.51 ± 1.90
BI-19	± 0.08	5	<i>MW</i> _{fiducial}	<i>MW</i> _{low}	600	0.12 ± 0.06	2.05 ± 0.54	6.92 ± 1.87
BI-20	± 0.12	5	<i>MW</i> _{fiducial}	<i>MW</i> _{low}	600	0.19 ± 0.09	2.69 ± 0.77	7.48 ± 1.91
BI-21	± 0.00	5	<i>MW</i> _{fiducial}	<i>MW</i> _{high}	600	0.01 ± 0.02	1.09 ± 0.14	0.10 ± 0.30
BI-22	± 0.04	5	<i>MW</i> _{fiducial}	<i>MW</i> _{high}	600	0.05 ± 0.04	1.46 ± 0.36	0.21 ± 0.44
BI-23	± 0.08	5	<i>MW</i> _{fiducial}	<i>MW</i> _{high}	600	0.14 ± 0.09	2.23 ± 0.80	0.77 ± 0.78
BI-24	± 0.12	5	<i>MW</i> _{fiducial}	<i>MW</i> _{high}	600	0.22 ± 0.12	2.91 ± 1.07	1.32 ± 0.94

Appendix B.2: Backward integration with MilkyWayPotential2022

In Fig. B.3, we re-ran some of our simulations and show a comparison between the backward integration done by MilkyWayPotential2022 from *Gala*. We found that our results remain qualitatively unchanged. In Fig. B.3, the first column corresponds to *MWPotential2014*, and the second to *MilkyWayPotential2022*. In each plot, we include one example with no proper motion error and one with a 0.04 mas/yr proper motion error. While some minor differences are noticeable, the overall behavior and results of our study remain unaffected by the choice of potential. We also tested a +40% halo mass variation for both *MWPotential2014* and *MilkyWayPotential2022*, and the results remained consistent.

Appendix B.3: Re-computing c/a but with test satellites within 300 kpc

Fig. B.4 shows the evolution of c/a for the *MW*_{fiducial} potential model, comparing cases with and without the exclusion of test satellites beyond 300 kpc. The dashed green line represents the backward evolution when these satellites are excluded, while the solid green line shows the backward evolution including all test particles. The black lines indicate the forward integration. The exclusion of satellites beyond 300 kpc does not significantly alter the overall evolution of c/a . While removing some test satellites has a minor effect on the backward integration of c/a , this effect is not substantial if satellites beyond 300 kpc are excluded.

Table A.3. Parameters and results for backward integration models at 3 Gyr in backward integration, similar to Table A.1 but at $\theta_{max} = 60^\circ$

Model	ϵ_μ [mas yr $^{-1}$]	ϵ_{dist} [%]	Potential		M_realization	$\Delta_{c/a}$	$f_{c/a}$	$N_{\text{sat}}(> 300 \text{ kpc})$
			Forward	Backward				
BI-01	± 0.00	0	MW_{fiducial}	MW_{fiducial}	600	0.00 ± 0.01	1.00 ± 0.10	1.20 ± 0.81
BI-02	± 0.04	0	MW_{fiducial}	MW_{fiducial}	600	0.06 ± 0.04	1.57 ± 0.39	1.19 ± 0.83
BI-03	± 0.08	0	MW_{fiducial}	MW_{fiducial}	600	0.16 ± 0.08	2.43 ± 0.74	1.66 ± 0.96
BI-04	± 0.12	0	MW_{fiducial}	MW_{fiducial}	600	0.24 ± 0.11	3.18 ± 0.99	2.34 ± 1.09
BI-05	± 0.00	0	MW_{fiducial}	MW_{low}	600	0.01 ± 0.03	1.07 ± 0.28	4.80 ± 1.50
BI-06	± 0.04	0	MW_{fiducial}	MW_{low}	600	0.05 ± 0.04	1.45 ± 0.34	5.19 ± 1.50
BI-07	± 0.08	0	MW_{fiducial}	MW_{low}	600	0.12 ± 0.07	2.11 ± 0.58	5.74 ± 1.54
BI-08	± 0.12	0	MW_{fiducial}	MW_{low}	600	0.20 ± 0.09	2.81 ± 0.8	6.15 ± 1.49
BI-09	± 0.00	0	MW_{fiducial}	MW_{high}	600	0.01 ± 0.02	1.05 ± 0.13	0.45 ± 0.50
BI-10	± 0.04	0	MW_{fiducial}	MW_{high}	600	0.07 ± 0.05	1.61 ± 0.42	0.52 ± 0.58
BI-11	± 0.08	0	MW_{fiducial}	MW_{high}	600	0.18 ± 0.09	2.58 ± 0.85	0.87 ± 0.77
BI-12	± 0.12	0	MW_{fiducial}	MW_{high}	600	0.25 ± 0.11	3.25 ± 0.95	1.39 ± 0.97
BI-13	± 0.00	5	MW_{fiducial}	MW_{fiducial}	600	0.02 ± 0.01	1.14 ± 0.12	1.35 ± 0.96
BI-14	± 0.04	5	MW_{fiducial}	MW_{fiducial}	600	0.07 ± 0.05	1.66 ± 0.42	1.53 ± 0.94
BI-15	± 0.08	5	MW_{fiducial}	MW_{fiducial}	600	0.17 ± 0.08	2.52 ± 0.76	2.28 ± 1.10
BI-16	± 0.12	5	MW_{fiducial}	MW_{fiducial}	600	0.24 ± 0.11	3.19 ± 0.96	2.98 ± 1.20
BI-17	± 0.00	5	MW_{fiducial}	MW_{low}	600	0.03 ± 0.04	1.26 ± 0.34	6.90 ± 1.76
BI-18	± 0.04	5	MW_{fiducial}	MW_{low}	600	0.06 ± 0.04	1.56 ± 0.36	7.38 ± 1.84
BI-19	± 0.08	5	MW_{fiducial}	MW_{low}	600	0.13 ± 0.06	2.15 ± 0.56	7.72 ± 1.86
BI-20	± 0.12	5	MW_{fiducial}	MW_{low}	600	0.21 ± 0.09	2.85 ± 0.81	8.09 ± 1.82
BI-21	± 0.00	5	MW_{fiducial}	MW_{high}	600	0.01 ± 0.01	1.09 ± 0.13	0.70 ± 0.64
BI-22	± 0.04	5	MW_{fiducial}	MW_{high}	600	0.08 ± 0.05	1.70 ± 0.46	0.76 ± 0.69
BI-23	± 0.08	5	MW_{fiducial}	MW_{high}	600	0.19 ± 0.09	2.67 ± 0.84	1.17 ± 0.84
BI-24	± 0.12	5	MW_{fiducial}	MW_{high}	600	0.26 ± 0.12	3.31 ± 1.07	1.82 ± 1.05

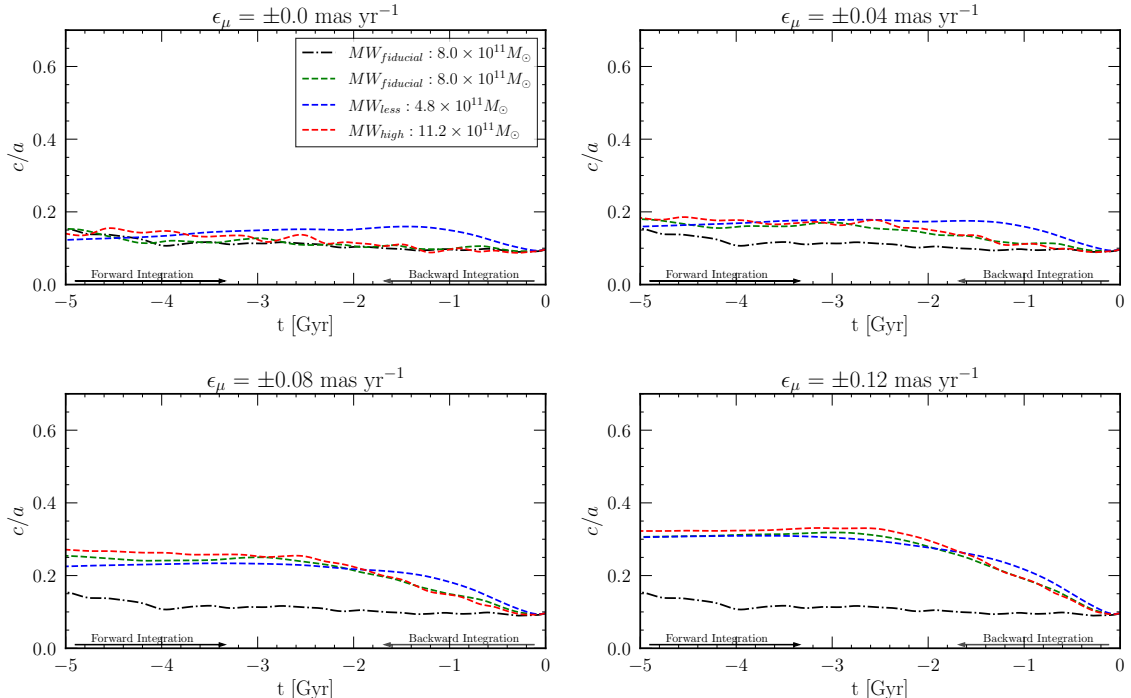


Fig. A.1. Analogous to Fig 7, results for $\theta_{tan} = 40^\circ$: Evolution of the plane of satellite galaxies with proper motion uncertainties included in each panel. The black dashed-dotted curves represent the mean axis ratio for forward integration, while the colored dashed curves indicate the mean axis ratio for backward integration under different potential models characterized by halo mass. Specifically, the blue, green, and red dashed curves correspond to the c/a values under the MW_{low} , MW_{fiducial} , and MW_{high} potential models, respectively. Note that in these results we account 5% of distance uncertainties.

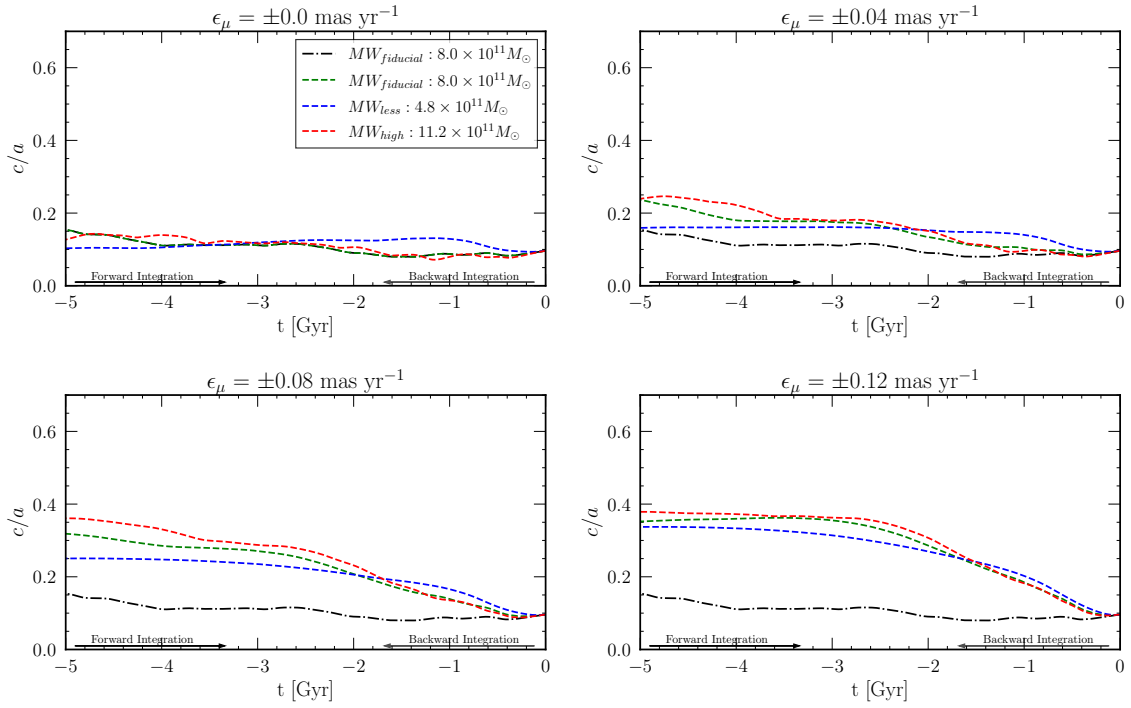


Fig. A.2. Analogous to Fig 6, results for $\theta_{tan} = 60^\circ$: Evolution of the plane of satellite galaxies with proper motion uncertainties included in each panel. The black dashed-dotted curves represent the mean axis ratio for forward integration, while the colored dashed curves indicate the mean axis ratio for backward integration under different potential models characterized by halo mass. Specifically, the blue, green, and red dashed curves correspond to the c/a values under the MW_{low} , $MW_{fiducial}$, and MW_{high} potential models, respectively. Note that these results do not account for distance uncertainties.

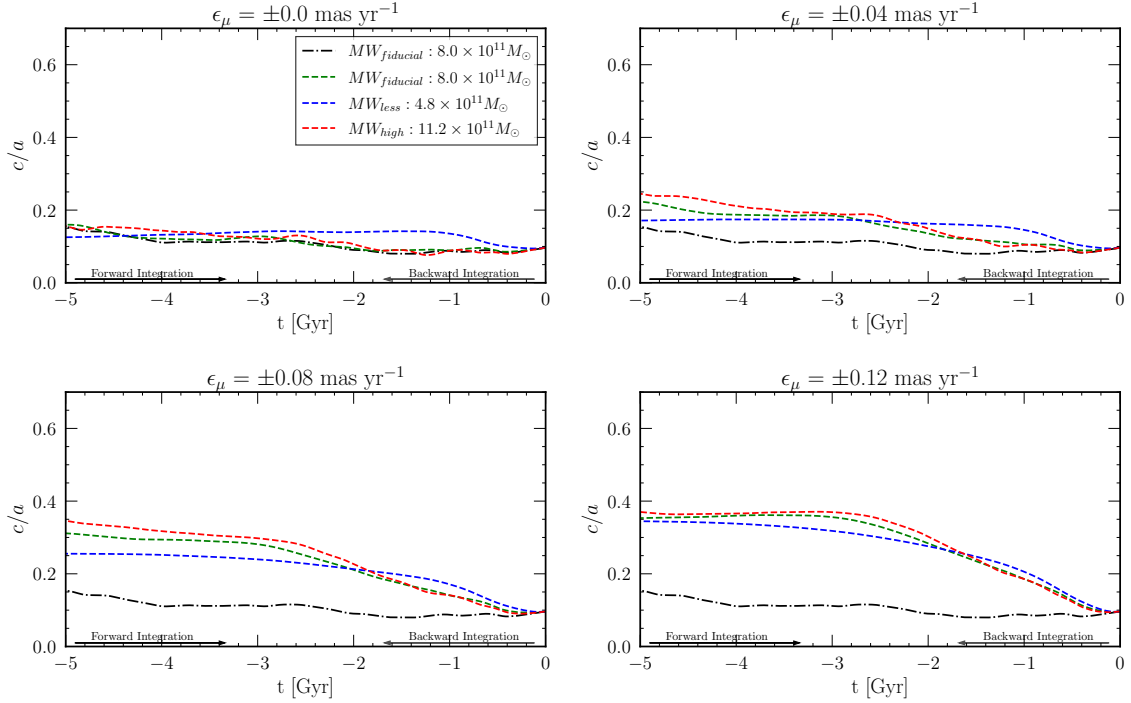


Fig. A.3. Analogous to Fig 7, results for $\theta_{tan} = 60^\circ$: Evolution of the plane of satellite galaxies with proper motion uncertainties included in each panel. The black dashed-dotted curves represent the mean axis ratio for forward integration, while the colored dashed curves indicate the mean axis ratio for backward integration under different potential models characterized by halo mass. Specifically, the blue, green, and red dashed curves correspond to the c/a values under the MW_{low} , $MW_{fiducial}$, and MW_{high} potential models, respectively. Note that in these results we account 5% of distance uncertainties.

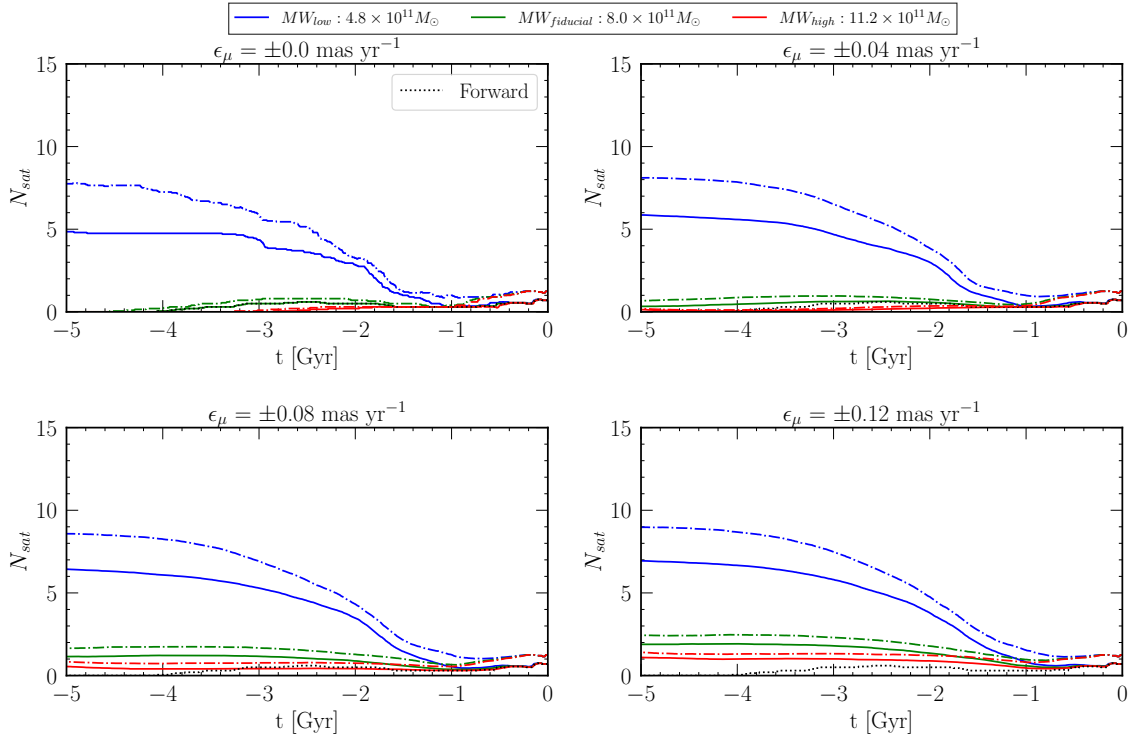


Fig. A.4. Average number of test satellite exceeding 300 kpc of radial distance under proper motion uncertainties. Similar to Fig. 9, but under $\theta_{tan} = 40^\circ$.

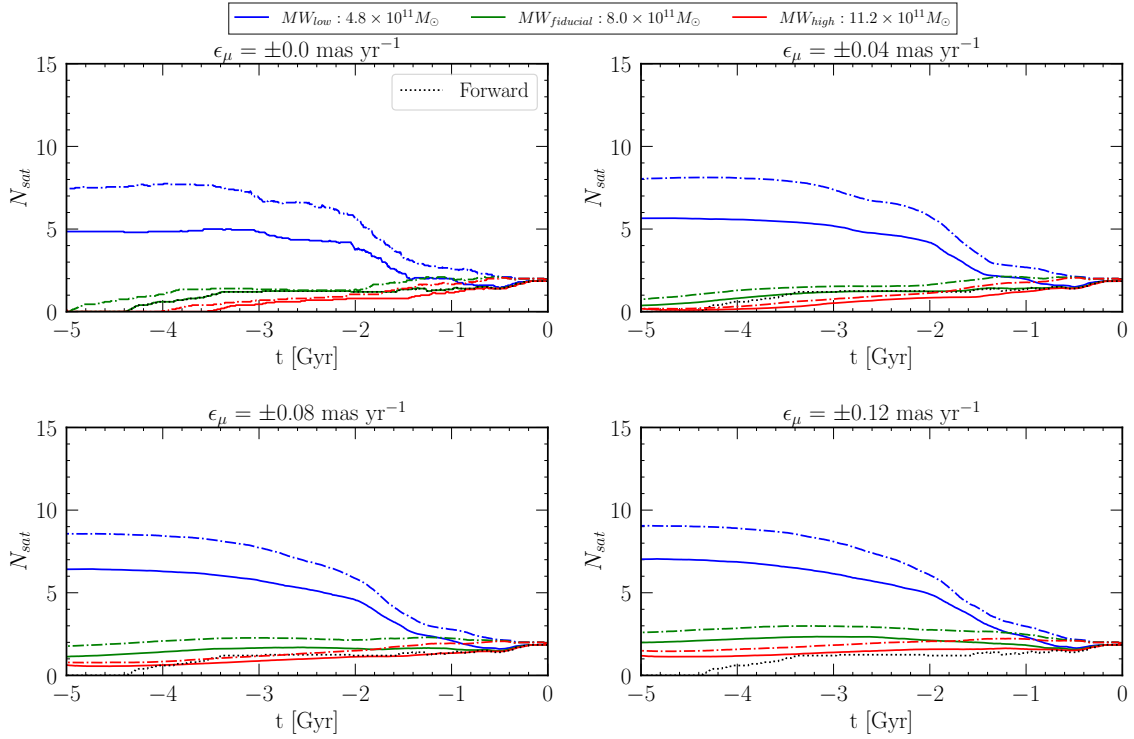


Fig. A.5. Average number of test satellite exceeding 300 kpc of radial distance under proper motion uncertainties. Similar to Fig. 9, but under $\theta_{tan} = 60^\circ$.

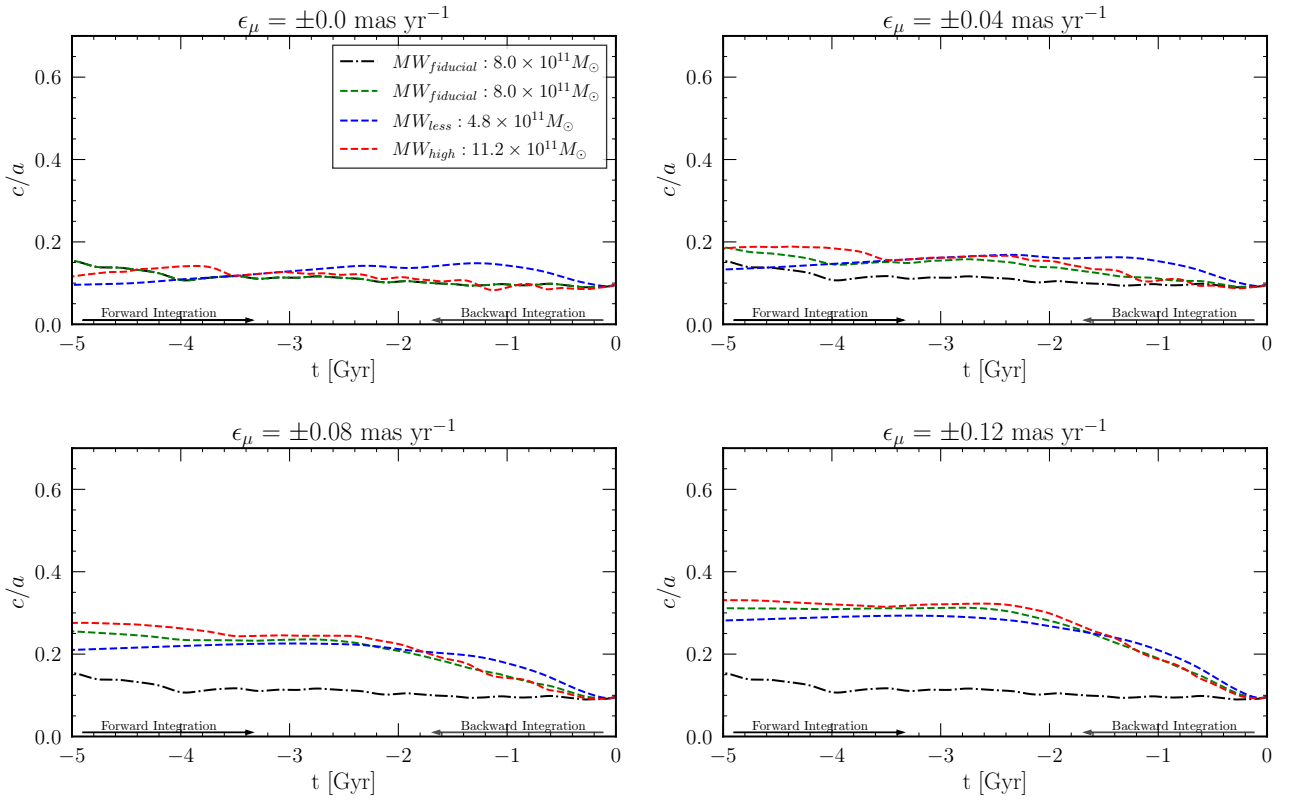


Fig. B.1. Analogous to Fig 6, the results for $\theta_{tan} = 40^\circ$: Evolution of the plane of satellite galaxies with proper motion uncertainties included in each panel. The black dashed-dotted curves represent the mean axis ratio for forward integration, while the colored dashed curves indicate the mean axis ratio for backward integration under different potential models characterized by halo mass. Specifically, the blue, green, and red dashed curves correspond to the c/a values under the MW_{low} , $MW_{fiducial}$, and MW_{high} potential models, respectively. Note that these results do not account for distance uncertainties.

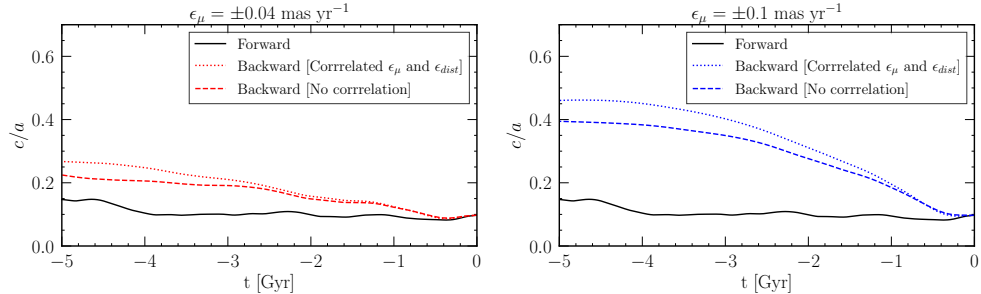


Fig. B.2. Comparison of correlated and uncorrelated PM-distance errors on satellite plane evolution. Two cases are shown with PM errors of 0.04 and 0.1 mas yr^{-1} , both with a 10% distance error. Correlated errors lead to a slightly increased plane widening.

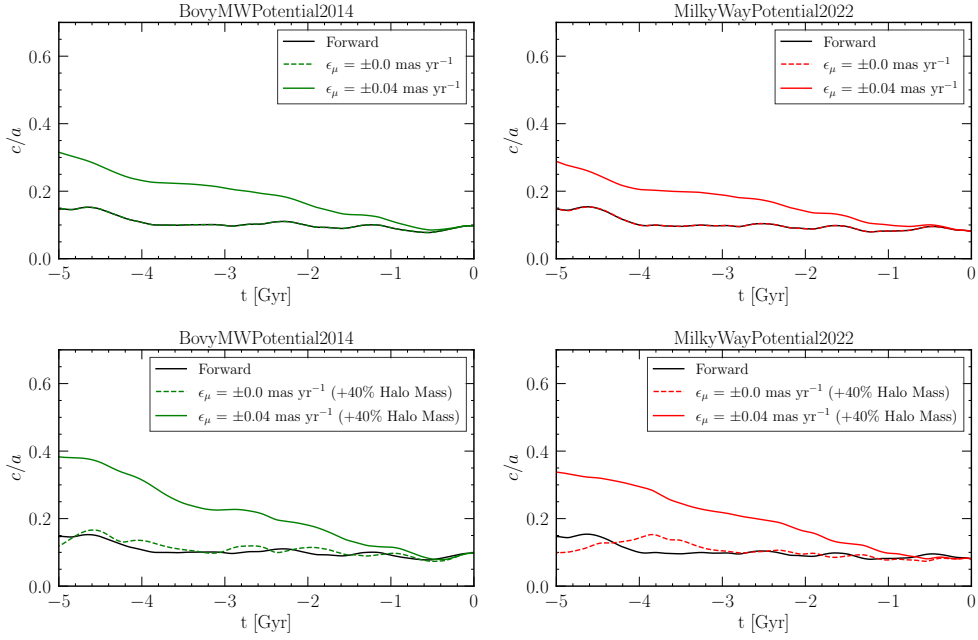


Fig. B.3. Comparison between MilkyWayPotential2022 and MWPotential2014

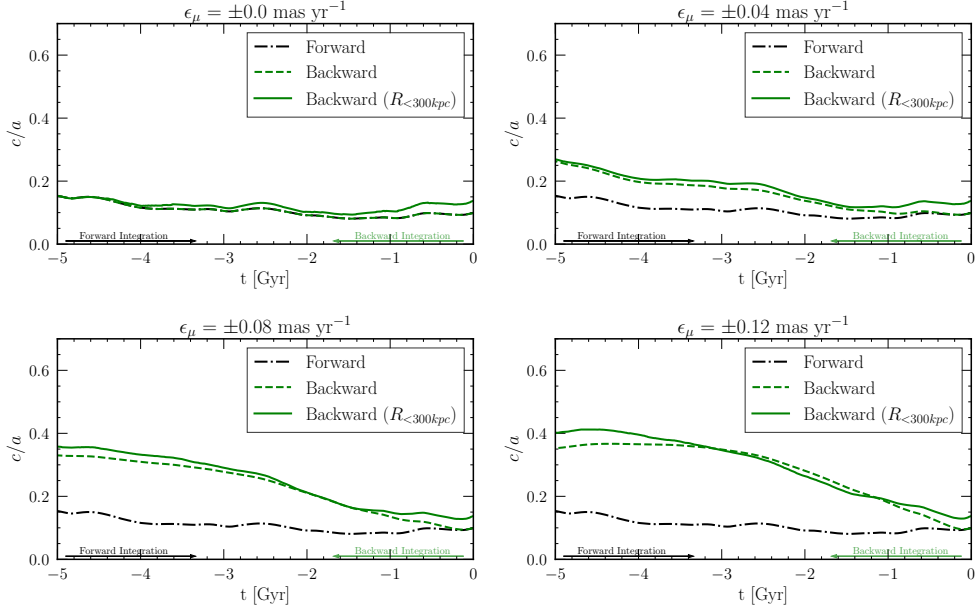


Fig. B.4. Evolution of c/a for the MW_{fiducial} model with and without excluding test satellites beyond 300 kpc. Dashed and solid green lines show backward evolution, black lines indicate forward integration. Exclusion has minimal impact on the overall trend.